Weighted Interior Penalty discretization of fully nonlinear and weakly dispersive free surface shallow water flows

Daniele Di Pietro, Fabien A Marche

Weighted Interior Penalty discretization of fully nonlinear and weakly dispersive free surface shallow water flows

Daniele A. Di Pietro*[1] and Fabien Marche†[1]

[1]University of Montpellier, Institut Montpelliérain Alexander Grothendieck, 34095 Montpellier, France

Abstract

In this paper, we further investigate the use of a fully discontinuous Finite Element discrete formulation for the study of shallow water free surface flows in the fully nonlinear and weakly dispersive flow regime. We consider a decoupling strategy in which we approximate the solutions of the classical shallow water equations supplemented with a source term globally accounting for the non-hydrostatic effects. This source term can be computed through the resolution of elliptic second-order linear sub-problems, which only involve second order partial derivatives in space. We then introduce an associated Symmetric Weighted Internal Penalty discrete bilinear form, allowing to deal with the discontinuous nature of the elliptic problem's coefficients in a stable and consistant way. Similar discrete formulations are also introduced for several recent optimized fully nonlinear and weakly dispersive models. These formulations are validated again several benchmarks involving h-convergence, p-convergence and comparisons with experimental data, showing optimal convergence properties.

Keywords: Green–Naghdi equations, discontinuous Galerkin, Internal Penalty methods, high-order schemes, free surface flows, shallow water equations, dispersive equations

1 Introduction

Considering a homogeneous incompressible and inviscid fluid, the propagation and transformation of free surface waves can be described using the Euler equations with nonlinear boundary conditions at the surface and at the bottom. In its full generality, this problem is very complicated to solve, both mathematically and numerically. For this reason, an important endeavour has been undertaken for the derivation and mathematical understanding of asymptotic models describing the behavior of the solution in some specific physical regimes; see, e.g., [32] for a review. We focus here on the *shallow water* and *fully nonlinear* regime:

$$\begin{aligned} &(\textit{shallow water regime}) \quad \mu := \frac{H_0^2}{\lambda^2} \ll 1, \\ &(\textit{large amplitude regime}) \quad \varepsilon := \frac{a}{H_0} = \mathcal{O}(1), \end{aligned} \tag{1}$$

where H_0 refers to the typical water depth, λ the typical wave length, and a the typical wave's amplitude. In this regime, the classical Nonlinear Shallow Water (NSW) equations can be derived from the full water waves equations by neglecting all the terms of order $\mathcal{O}(\mu)$, see for instance [31]. This model provides an accurate description of important unsteady processes in the surf and swash zones, such as nonlinear wave transformations, run-up and flooding due to storm waves, see for instance [6], but it neglects the dispersive effects which are fundamental for the study of wave transformations in the shoaling area and, possibly, slightly deeper water areas. The corresponding equations where $\mathcal{O}(\mu)$ terms are not neglected were first derived by Serre [47] in the horizontal surface dimension, then by Green and Naghdi [27] for the two-dimensional case, and have been recently mathematically justified in [3].

*daniele.di-pietro@umontpellier.fr
†Fabien.Marche@umontpellier.fr

Focusing on the one dimensional (horizontal) case, let x, z, and t denote, respectively, the horizontal, vertical, and time coordinates. We denote by $\zeta(t,x)$ the free surface elevation with respect to its rest state, by $-H_0+b(x)$ a parametrization of the bottom's variations, by $H := H_0+\zeta-b$ the water depth, and by $\eta = H+b$ the total free surface elevation, as shown in Figure 1. Denoting by $\mathbf{u}_{\rm hor}$ the horizontal component of the velocity field in the fluid domain, we define the vertically averaged horizontal velocity $u \in \mathbb{R}$ as

$$u(t,x) := \frac{1}{H}\int_{-H_0+b}^{\zeta} \mathbf{u}_{\rm hor}(t,x,z)dz,$$

and we denote by $q := Hu$ the corresponding horizontal momentum. The classical Green–Naghdi (GN) equations read as follows:

$$\begin{aligned} \partial_t\zeta + \partial_x(Hu) &= 0, \\ \left(1+\mathcal{T}[H,b]\right)\partial_t u + u\partial_x u + g\partial_x\zeta + \mathcal{Q}[H,b](u) &= 0, \end{aligned} \tag{2}$$

where the linear operator $\mathcal{T}[H,b]\cdot$ and the quadratic form $\mathcal{Q}[H,b](\cdot)$ are defined for all smooth enough scalar-valued functions w by

$$\begin{aligned} \mathcal{T}[H,b]w &:= \mathcal{R}_1[H,b](\partial_x w) + \mathcal{R}_2[H,b](w\partial_x b), \\ \mathcal{Q}[H,b](w) &:= \mathcal{R}_1[H,b](\partial_x(w\partial_x w) - 2(\partial_x w)^2) + \mathcal{R}_2[H,b]((w\partial_x)^2 b), \end{aligned}$$

where

$$\mathcal{R}_1[H,b]w := -\frac{1}{3H}\partial_x(H^3 w) - \frac{H}{2}w\partial_x b, \qquad \mathcal{R}_2[H,b]w := \frac{1}{2H}\partial_x(H^2 w) + w\partial_x b.$$

The numerical approximation of the GN equations has only been considered in recent years, and several methods have been proposed in one space dimension, including: Finite Differences (FD) [1, 50], Finite Volumes (FV) [13, 34], hybrid FV-FD or WENO-FD methods [7, 8, 11], continuous Finite-Elements (CG) [25, 40, 41, 51] or even pseudo-spectral methods (SM) [24]. The two-dimensional case has received less attention and, besides the pioneering FD approaches of [4], we can cite the pseudo-spectral method for the rotating case developed in [43], the hybrid FV-FD approaches pf [44, 48], and the WENO-FD strategy of [33] on Cartesian meshes. It is also worth mentioning here some related works concerning *non-hydrostatic* models [2, 12], or the so called high-level GN equations [55].

Recently, discontinuous Finite-Element (DG) discretizations of the Green–Naghdi equations have also been considered. The use of DG methods for free surface flows is an interesting alternative to FV and CG approximations for several reasons: (i) as in CG methods, accuracy can be improved by increasing the polynomial order within an element rather than by enlarging the stencil; (ii) upwinding and stability post-processing can be incorporated into the solution through the resolution of local Riemann problems, which is particularly well-suited to model the highly advective free surface flows under study; (iii) adaptive strategies can be easily implemented through nonconforming mesh refinement or by locally adapting the polynomial degree (possibly in an independent manner for each variable and mesh element). This is a particularly attractive feature when performing computations in complex domains, or when dealing with flows involving highly local processes, like wave shoaling, wave breaking, or run-up and submersion; (iv) the mass equation is satisfied in a weak sense element by element. This property is particularly useful when coupling the GN equations to transport equations, bottom evolution models, or even floating body evolution laws; (v) domain decomposition strategies can be efficiently implemented thanks to the compact stencils and the minimal inter-elements exchanges, making DG methods highly parallelizable. In the one-dimensional case, we can refer to [37] for a hybrid centred DG-CG approach, and to [22, 42] for nonconforming approaches, while the two-dimensional case on unstructured meshes has recently been addressed in [23], partly motivated by the need to model free surface flows in complex domains. More precisely, in [22, 23], a decoupling strategy between the "hyperbolic" and "elliptic" parts of the equations is implemented and the authors consider the NSW equations supplemented by an additional algebraic source term accounting for the dispersive correction, which is obtained through the approximate resolution of elliptic second order linear problems. The discrete formulation associated with $\mathcal{T}[H,b]$ is built using a mixed formulation, relying on the *Local discontinuous Galerkin* (LDG) method [14].

In the present work, we further investigate the numerical resolution of fully nonlinear and weakly dispersive free surface flow equations with non-conforming methods. Reformulating the regularizing operator

$\mathcal{T}[H,b]$ so that it only involves second order derivatives in space, we construct a symmetric discrete bilinear form directly associated with the primal form of the auxiliary elliptic problems. We focus, in particular, on the *Weighted Symmetric Internal Penalty* (SWIP) method (see [18] and references therein), which is designed so that the stability threshold on the penalty parameter is independent of the interface values of H and b. Concerning the discretization of the nonlinear operator $\mathcal{Q}[H,b]$, we introduce a discrete gradient operator inspired by [16] and a discrete Laplace operators inspired by [30], both accounting for the nonconformity of the discrete functions. Similar discrete formulations are also constructed for the optimized Green-Naghdi equations introduced in [33]. A thorough numerical validation of the proposed method is carried out. The numerical tests show convergence with optimal orders even on varying bottom. We also study p-convergence and show that for the considered test cases, the expected exponential convergence is observed for a fixed meshsize h.

The rest of this work is organized as follows: we recall some recent equivalent shallow water asymptotic models and associated notations in section Section 2, while Section 3 is devoted to the introduction of the discrete settings and the DG formulations. This approach is then validated in Section 4 through convergence analysis and comparisons with data taken from experiments on several discriminating benchmark problems. Several elements of comparisons between the asymptotic models under study are also provided.

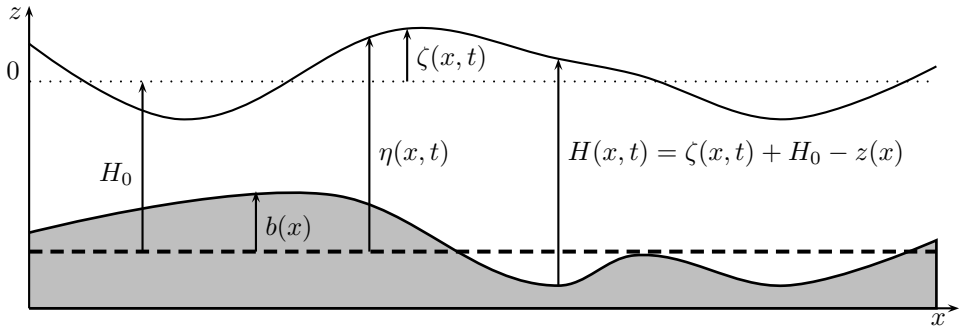

Figure 1: Main notations

2 Shallow water asymptotics

2.1 Model 1: Green–Naghdi

Following [8, 22], the Green–Naghdi equations can be written using (η, q) as flow variables as follows:

$$\begin{aligned} \partial_t \eta + \partial_x q &= 0\,, \\ (1 + \mathbf{T}[H,b])\,(\partial_t q + \partial_x(uq)) + gH\partial_x\zeta + H\mathcal{Q}_1[H,b](u) &= 0\,, \end{aligned} \tag{3}$$

where the linear operator $\mathbf{T}[H,b]\cdot$ and the quadratic form $\mathcal{Q}_1[H,b](\cdot)$ are defined for all smooth enough scalar-valued functions w by

$$\mathbf{T}[H,b]w := H\mathcal{T}[H,b]\frac{w}{H}, \tag{4}$$

$$\mathcal{Q}_1[H,b](w) := -2\mathcal{R}_1[H,b]((\partial_x w)^2) + \mathcal{R}_2[H,b]((w\partial_x)^2 b). \tag{5}$$

Denoting by $\mathbf{w} := (\eta, q)$ the vector collecting the primal variables, using the following *pre-balanced* splitting of the hydrostatic pressure term (see [35]):

$$gH\partial_x\zeta = \frac{1}{2}g\partial_x(\eta^2 - 2\eta b) + g\eta\partial_x b, \tag{6}$$

and introducing an auxiliary variable $\mathfrak{d}$, we obtain our first model:

Model 1 (Green–Naghdi)**.**

$$\partial_t \mathbf{w} + \partial_x \mathbb{f}(\mathbf{w}, b) + \mathbb{d}(\mathbf{w}, b) = \mathbb{b}(\mathbf{w}, b), \tag{7a}$$
$$(1+\mathbf{T}[H, b])(\mathfrak{d} + gH\partial_x \eta) = gH\partial_x \eta + H\mathcal{Q}_1[H, b](u), \tag{7b}$$

where

$$\mathbb{f}(\mathbf{w}, b) := \begin{pmatrix} q \\ \mathfrak{f}(\mathbf{w}, b) \end{pmatrix}, \quad \mathbb{b}(\mathbf{w}, b) := \begin{pmatrix} 0 \\ -g\eta\partial_x b \end{pmatrix}, \quad \mathbb{d}(\mathbf{w}, b) := \begin{pmatrix} 0 \\ \mathfrak{d} \end{pmatrix}, \tag{8}$$

and the nonlinear *pre-balanced* flux is defined as

$$\mathfrak{f}(\mathbf{w}, b) := \frac{q^2}{H} + \frac{1}{2} g\partial_x(\eta^2 - 2\eta b).$$

Model 1 is equivalent to (2), and highlights the fact that the Green–Naghdi equations can be regarded as a dispersive correction of order $\mathcal{O}(\mu)$ of the nonlinear hyperbolic shallow water equations. This dispersive correction corresponds to the source term $\mathbb{d}(\mathbf{w}, b)$ in (7a), and is obtained as the solution of an auxiliary scalar and linear second-order elliptic sub-problem (7b). This formulation does not require the computation of third order derivatives and, as shown in the theoretical analysis of [3] and in our previous works [8, 11, 22], the presence of the operator $(1 + \mathbf{T}[H, b])^{-1}$ makes the model robust with respect to high frequency perturbations. When $b = 0$, Model 1 admits solitary wave solutions of amplitude εH_0, which have known formulae in a closed form:

$$\eta(x, t) = H_0 + \varepsilon H_0 \operatorname{sech}^2(\kappa(x - ct)), \qquad q(x, t) = c(\eta(t, x) - H_0), \tag{9}$$

with $\kappa := \sqrt{\frac{3\varepsilon}{4H_0^2(1+\varepsilon)}}$ and $c := \sqrt{gH_0(1+\varepsilon)}$. It also has a Hamiltonian structure, ensuring the exact conservation of the total energy:

$$\frac{d}{dt} E(t) = 0, \qquad E(t) := \int_{\mathbb{R}} g\zeta^2 + H|u|^2 + H(\mathcal{T}[H, b]u(t, x))u(t, x)\, dx. \tag{10}$$

Remark 1 (Well-posedeness for the Green–Naghdi model)**.** Model 1 is rigorously justified in [3], where a well-posedness result is proved for the general two-dimensional case with varying bottom using a Nash–Moser scheme. This result has also been obtained using a Picard iterative scheme in the one-dimensional case in [29]. More precisely, assuming that $(\eta_0, u_0) \in H^s(\mathbb{R}) \times H^{s+1}(\mathbb{R})$ with $s > \frac{3}{2}$ (where $H^s(\mathbb{R})$ is the Sobolev space of functions $v \in L^2(\mathbb{R})$ such that their weak derivatives up to order s have a finite L^2-norm) and that $b \in \mathcal{C}_b^\infty(\mathbb{R})$ (where $\mathcal{C}_b^\infty(\mathbb{R})$ is the space of infinitely differentiable functions that are bounded together with all their derivatives), then there exists a maximal time $t_{\max} > 0$, uniformly bounded with respect to μ, such that Model 1 admits a unique solution $(\eta, u) \in \mathcal{C}([0, t_{\max}], H^s(\mathbb{R}) \times H^{s+1}(\mathbb{R}))$. This result can be extended to finite domains and periodic boundary conditions.

2.2 Model 2: Modified Green–Naghdi

In Model 1, the quantity $(1+\mathbf{T}[H, b])$ appearing in (7b) is a time dependent operator. From the numerical point of view, this means that the computation of the dispersive correction requires the assembly and inversion of the corresponding matrix at each time step or sub-step. To avoid this computationally intensive operation, a new asymptotically equivalent model has been introduced in [33]. Define the (time-independent) water depth at rest as follows:

$$H^b := H_0 - b.$$

The modified Green–Naghdi equations read

$$\partial_t \eta + \partial_x q = 0,$$
$$\left(1 + \mathbb{T}[H^b]\right)(\partial_t q + \partial_x(uq)) + gH\partial_x \zeta + \mathbb{Q}[H, b](\zeta, u) = 0,$$

where, for any smooth enough $\mathbb{R}$-valued function w,

$$\mathbb{T}[H^b]w := -\mathcal{D}[H^b]\frac{w}{H^b}, \tag{11}$$

with

$$\mathcal{D}[H]w := \frac{1}{3}\partial_x\left(H^3\partial_x w\right), \tag{12}$$

and

$$\mathbb{Q}[H,b](\zeta,w) := H(\mathcal{Q}_1[H,b](w) + g\mathcal{Q}_2[H,b](\zeta)) + \mathcal{Q}_3[H,H^b]\left(\left[1+\mathbb{T}[H^b]\right]^{-1}(gH\partial_x\zeta)\right),$$

is a second order nonlinear operator with

$$\mathcal{Q}_2[H,b](\zeta) := -\frac{1}{2H}\partial_x(H^2\partial_x b\partial_x\zeta) + \left(\frac{H}{2}\partial_x^2\zeta - (\partial_x b\partial_x\zeta)\right)\partial_x b,$$

and, for all smooth enough $\mathbb{R}$-valued functions w,

$$\mathcal{Q}_3[H,H^b]w := \frac{1}{6}\partial_x(H^2-(H^b)^2)\partial_x w + \frac{H^2-(H^b)^2}{3}\partial_x^2 w - \frac{1}{6}\partial_x^2(H^2-(H^b)^2)w.$$

Recalling that $\mathbf{w} := (\eta, q)$ collects the primal variables, using again (6), and introducing two novel auxiliary variables $\mathfrak{d}$ and $\mathfrak{q}$, we obtain the following model:

Model 2 (Modified Green–Naghdi)**.**

$$\begin{aligned}
\partial_t\mathbf{w} + \partial_x\mathbb{f}(\mathbf{w},b) + \mathbb{d}(\mathbf{w},b) &= \mathbb{b}(\mathbf{w},b),\\
\left(1+\mathbb{T}[H^b]\right)(\mathfrak{d} + gH\partial_x\eta) &= H(g\partial_x\eta + \mathcal{Q}_1[H,b](u) + g\mathcal{Q}_2[H,b](\eta)) + \mathcal{Q}_3[H,H^b]\mathfrak{q},\\
\left(1+\mathbb{T}[H^b]\right)\mathfrak{q} &= gH\partial_x\eta,
\end{aligned} \tag{13}$$

where $\mathbb{f}(\mathbf{w},b)$, $\mathbb{d}(\mathbf{w},b)$, and $\mathbb{b}(\mathbf{w},b)$ are defined by (8).

Model 2 preserves the $\mathcal{O}(\mu^2)$ asymptotic consistency with the free surface Euler equations. In contrast, it is only asymptotically equivalent to Model 1 up to $\mathcal{O}(\mu^2)$ terms appearing in the momentum equation. As a consequence, it does not admit the solitary wave solutions given in closed form by (9), and the energy (10) is only preserved up to $\mathcal{O}(\mu^2)$ terms. Using Model 2 as a starting point for the discretization has two key advantages: (i) the discrete version of the operator $(1+\mathbb{T}[H^b])$ appearing in the equations defining the dispersive terms can be assembled and factorized once and for all, in a preprocessing step; (ii) the quadratic term $\mathbb{Q}[H,b]$ does not require the computation of third order derivatives. The presence of third order derivatives can lead to high frequency instabilities, and it has been shown in [25] that, when third order derivatives on the free surface occur, it is important to introduce some sophisticated approximation strategies for the free surface gradient to reduce the dispersion error. As shown in [33], these favorable features come at the price of an extra linear system to invert. In practice, this cost is largely off-set by the gain obtained by using the time independent operator $\mathbb{T}[H^b]$.

2.3 Model 3: Optimized Green–Naghdi

Following [33], it is possible to improve the dispersive properties of Model 2 without modifying its asymptotic accuracy. This can be achieved by introducing three parameters α, θ, γ and considering the following change of variables for the velocity:

$$\forall\theta \geq 0, \quad u := \left(1 - \frac{\theta}{H}\mathcal{D}[H]\right)u^\theta.$$

The three-parameters optimized Green–Naghdi equations of [33] read

$$\begin{aligned}
\left(1+\gamma\mathbb{T}[H^b]\right)\left(\partial_t\zeta + \partial_x(Hu^\theta)\right) - \theta\partial_x\left(\mathcal{D}[H]u^\theta\right) &= 0,\\
\left(1+\alpha(1+\theta)\mathbb{T}[H^b]\right)\left(\partial_t(Hu^\theta) + \partial_x(Hu^{\theta^2}) + \frac{\alpha-1}{\alpha}gH\partial_x\zeta\right) + \frac{1}{\alpha}gH\partial_x\zeta + \tilde{\mathbb{Q}}[H,b](\zeta,u^\theta) &= 0,
\end{aligned}$$

where, for any smooth enough scalar valued functions w,

$$\tilde{\mathbb{Q}}[H,b](\zeta,w) := H(\mathcal{Q}_1[H,b](w) + g\mathcal{Q}_2[H,b](\zeta)) \\ + (1+\theta)\mathcal{Q}_3[H,H^b]\left(\left(1+\alpha(1+\theta)\mathbb{T}[H^b]\right)^{-1}(gH\partial_x\zeta)\right) + \theta\mathcal{Q}_4[H]w,$$

and

$$\mathcal{Q}_4[H]w := -\partial_x\left(\mathcal{D}[H]w\right)w + \frac{2}{3}H^2\partial_x(Hw)\partial_x^2 w + H\partial_x(H\partial_x(Hw))\partial_x u \\ + \frac{2}{3}H^3\partial_x w\partial_x^2 w + Hw\partial_x\left(H\partial_x H\right)\partial_x w.$$

Using again (6), letting $\mathbf{w}^\theta = (\eta, q^\theta)$ with $q^\theta = Hu^\theta$ denote the vector of primal variables, and introducing three auxiliary variables $\mathfrak{d}, \mathfrak{q}$ and $\mathfrak{r}$, we arrive at

Model 3 (Optimized Green–Naghdi)**.**

$$\begin{aligned}
\partial_t\mathbf{w}^\theta + \partial_x\mathbb{f}(\mathbf{w}^\theta,b) + \mathbb{d}^{\alpha,\gamma,\theta}(\mathbf{w}^\theta,b) &= \mathbb{b}(\mathbf{w}^\theta,b),\\
\left(1+\alpha(1+\theta)\mathbb{T}[H^b]\right)\left(\mathfrak{d} + \frac{1}{\alpha}gH\partial_x\eta\right) &= H(\frac{1}{\alpha}g\partial_x\eta + \mathcal{Q}_1[H,b](u^\theta) + g\mathcal{Q}_2[H,b](\eta))\\
&\quad + (1+\theta)\mathcal{Q}_3[H,H^b]\mathfrak{q} + \theta\mathcal{Q}_4[H]u^\theta,\\
\left(1+\alpha(1+\theta)\mathbb{T}[H^b]\right)\mathfrak{q} &= gH\partial_x\eta,\\
\left(1+\gamma\mathbb{T}[H^b]\right)\mathfrak{r} + \theta\partial_x\Big(\mathcal{D}[H]u^\theta\Big) &= 0,
\end{aligned}$$

with dispersive correction $\mathbb{d}^{\alpha,\gamma,\theta}(\mathbf{w}^\theta,b) := \begin{pmatrix}\mathfrak{r}\\ \mathfrak{d}\end{pmatrix}$, $\mathbb{f}(\mathbf{w}^\theta,b)$ and $\mathbb{b}(\mathbf{w}^\theta,b)$ defined in (8), and $\mathcal{D}[H]$ defined by (12).

The interest of working with Model 3 is that the parameters can be carefully tuned to optimize the dispersive properties with respect to the properties of the free surface Euler equations; see [11, 33] for more details and Section 4.2.2 for an example of optimization. Additionally, for given values of α, γ, θ, the discrete versions of both the operators $\left(1+\gamma\mathbb{T}[H^b]\right)$ and $\left(1+\alpha(1+\theta)\mathbb{T}[H^b]\right)$ can be assembled and factorized once and for all, in a preprocessing step. It can be shown that Model 3 is asymptotically equivalent to Model 2 up to $\mathcal{O}(\mu^2)$ terms appearing both in the mass and momentum equations. In particular, Model 2 can be recovered setting $\alpha = 1$ and $\gamma = \theta = 0$. Model 3 does not admit solitary wave solutions in the closed form (9), and both mass and energy are conserved only up to $\mathcal{O}(\mu^2)$ terms. A difference with Model 2 is the presence of third order spatial derivatives of the velocity u^θ, occurring both in $\mathcal{Q}_4[H]$ and $\partial_x\left(\mathcal{D}[H]u^\theta\right)$.

3 Discrete formulations

In this section, we derive Discontinuous Galerkin approximations of the three models discussed above. Although we work here in one space dimension, we keep the notation as close as possible to the classical one for DG methods in higher space dimensions; see, e.g., [17]. This is both to facilitate the reader familiar with Discontinuous Galerkin methods, and to facilitate the extension to two space dimensions, which we postpone to a future work.

3.1 Setting and notations

Let $\Omega \subset \mathbb{R}$ denote an open segment with boundary $\partial\Omega$. We consider a partition $\mathcal{T}_h$ of Ω in open disjoint segments T of boundary ∂T such that $\overline{\Omega} = \bigcup_{T\in\mathcal{T}_h}\overline{T}$. The partition is characterized by the meshsize $h := \max_{T\in\mathcal{T}_h} h_T$, where h_T is the length of the element T. For all $T \in \mathcal{T}_h$, we denote by n_T the unit outward normal taking values in $\{-1, 1\}$ on ∂T, and by x_T its barycenter.

Mesh faces, reduced here to vertices, are collected in the set $\mathcal{F}_h$ partitioned as $\mathcal{F}_h = \mathcal{F}_h^{\mathrm{i}} \cup \mathcal{F}_h^{\mathrm{b}}$, where $\mathcal{F}_h^{\mathrm{i}}$ collects the internal vertices and $\mathcal{F}_h^{\mathrm{b}}$ the (two) boundary vertices. The abscissa of a vertex $F \in \mathcal{F}_h$ is

denoted by x_F, and we let h_F denote the minimum length of the mesh elements to which F belongs. For all $T \in \mathcal{T}_h$, $\mathcal{F}_T := \{F \in \mathcal{F}_h \mid F \subset \partial T\}$ denotes the set of vertices in ∂T and, for all $F \in \mathcal{F}_T$, n_{TF} is the unit normal to F pointing out of T. For any internal vertex $F \in \mathcal{F}_h^{\mathrm{i}}$, we choose an arbitrarily oriented but fixed unit normal n_F, and we set $\mathrm{n}_F := \mathrm{n}_{TF}$ for all boundary vertices $F \subset \partial T \cap \partial\Omega$.
Given an integer polynomial degree $k \geq 1$, we consider the broken polynomial space

$$\mathbb{P}^k(\mathcal{T}_h) := \left\{v \in L^2(\Omega) \,|\, v_{|T} \in \mathbb{P}^k(T) \;\forall T \in \mathcal{T}_h\right\}, \tag{14}$$

where $\mathbb{P}^k(T)$ denotes the space of polynomials in T of total degree at most k.

For a given final computational time $t_{\max} > 0$, we consider a partition $(t^n)_{0\leq n\leq N}$ of the time interval $[0, t_{\max}]$ with $t^0 = 0$, $t^N = t_{\max}$ and $t^{n+1} - t^n =: \Delta t^n$. More details on the computation of the time step Δt^n and on the time marching algorithms are given in Section 3.5. For any sufficiently regular scalar-valued function of time w, we let $w^n := w(t^n)$.

Finally, we introduce the following shortcut notations for smooth enough scalar-valued functions v, w:

$$\left(v, w\right)_\Omega := \int_\Omega v(x)w(x)dx, \quad \left(v, w\right)_T := \int_T v(x)w(x)dx \quad \forall T \in \mathcal{T}_h, \quad \left(v, w\right)_F := (vw)(x_F) \quad \forall F \in \mathcal{F}_h.$$

3.2 Symmetric weighted penalty diffusion bilinear form

Let $\kappa \in L^\infty(\Omega)$ de note a uniformly positive coefficient and set, for the sake of brevity, $\kappa_T := \kappa_{|T}$ for all $T \in \mathcal{T}_h$. Following [18,20], we define the jump and weighted average operators such that, for a sufficiently smooth function φ and an interior vertex $F \in \mathcal{F}_h^i$ such that $F \subset \partial T_1 \cap \partial T_2$ for distinct mesh elements T_1 and T_2,

$$[\![\varphi]\!] := \varphi_{|T_1} - \varphi_{|T_2}, \qquad \{\!\{\varphi\}\!\}_{\omega,F} := \omega_2\varphi_{|T_1} + \omega_1\varphi_{|T_2}, \quad \omega_i := \frac{\kappa_{T_i}}{\kappa_{T_1} + \kappa_{T_2}} \quad \forall i \in \{1, 2\}. \tag{15}$$

In what follows, and when no confusion can arise, we omit the subscript F from both $[\![v]\!]_{\omega,F}$ and $\{\!\{v\}\!\}_{\omega,F}$. When $\kappa \equiv C$ in Ω for some real number $C > 0$, we have $\omega_1 = \omega_2 = \frac{1}{2}$, and also the subscript ω is omitted. The definition of the average and jump operators at boundary vertices depends on the selected boundary condition. When considering periodic boundary conditions, the two boundary vertices can be regarded as an additional internal vertex $F_{\mathrm{b}} \in \mathcal{F}_h^i$ defined as the intersection of the boundaries of the first and last elements of the mesh. The average and jump operators $\{\!\{\cdot\}\!\}_{\omega,F_{\mathrm{b}}}(x)$ and $[\![\cdot]\!]_{F_{\mathrm{b}}}$ at this fictitious interface are then defined accordingly. We refer the reader to [17, Section 4.5] for a discussion on the role of weighted averages and harmonic means in the context of heterogeneous diffusion problems.

For further use, we consider the following diffusive bilinear form $a_h(\kappa;\cdot,\cdot)$ on $\mathbb{P}^k(\mathcal{T}_h) \times \mathbb{P}^k(\mathcal{T}_h)$:

$$\begin{aligned} a_h(\kappa; v_h, w_h) := &\sum_{T\in\mathcal{T}_h} \left(\kappa\partial_x v_h, \partial_x w_h\right)_T + \sum_{F\in\mathcal{F}_h} \left(\frac{\xi_{\kappa,F}}{h_F}[\![v_h]\!], [\![w_h]\!]\right)_F \\ &- \sum_{F\in\mathcal{F}_h} \left(\left(\{\!\{\kappa\partial_x^h v_h\}\!\}_\omega, [\![w_h]\!]\right)_F + \left([\![v_h]\!], \{\!\{\kappa\partial_x^h w_h\}\!\}_\omega\right)_F\right), \end{aligned}$$

with diffusion-dependent penalty coefficient

$$\xi_{\kappa,F} := \begin{cases} \xi\frac{2\kappa_{T_1}\kappa_{T_2}}{\kappa_{T_1}+\kappa_{T_2}} & \text{if } F \in \mathcal{F}_h^{\mathrm{i}} \text{ is such that } F = \partial T_1 \cap \partial T_2, \\ \xi\kappa_T & \text{if } F \in \mathcal{F}_h^{\mathrm{b}} \text{ is such that } F = \partial T \cap \partial\Omega, \end{cases}$$

where ξ denotes a user-defined parameter sufficiently large to ensure coercivity (see, e.g., [17, Lemmas 4.12 and 4.51]). Notice that, in (3.2), ∂_x^h has to be intended as the broken partial derivative along x on $\mathcal{T}_h$.

3.3 Discrete gradient and Laplace operators

To discretize the linear and nonlinear operators that appear in our models, we need discrete counterparts of the gradient and of the Laplacian applied to broken polynomial functions. For any $v_h \in \mathbb{P}^k(\mathcal{T}_h)$, we

define the following global lifting of the jumps of v_h (see, e.g. [17, Section 4.3]):

$$\mathcal{R}_h^k([\![v_h]\!]) := \sum_{F\in\mathcal{F}_h} r_F^k([\![v_h]\!]),$$

where, for all $F \in \mathcal{F}_h$, the local lifting operator $r_F^k([\![v_h]\!]) \in \mathbb{P}^k(\mathcal{T}_h)$ is defined as the unique solution of the following problem:

$$\big(r_F^k([\![v_h]\!]), \psi_h\big)_\Omega = \big([\![v_h]\!], \{\!\{\psi_h\}\!\}\mathrm{n}_F\big)_F \qquad \forall \psi_h \in \mathbb{P}^k(\mathcal{T}_h),$$

with $\{\!\{\psi_h\}\!\}$ standard average operators given by (15) with $\omega_1 = \omega_2 = \frac{1}{2}$ at internal nodes and extended as described in the previous section to boundary nodes. Following [17, Section 2.3], we define the discrete gradient operator $\mathcal{G}_h^k : \mathbb{P}^k(\mathcal{T}_h) \to \mathbb{P}^k(\mathcal{T}_h)$ such that, for all $v_h \in \mathbb{P}^k(\mathcal{T}_h)$,

$$\mathcal{G}_h^k(v_h) := \partial_x^h v_h - \mathcal{R}_h^k([\![v_h]\!]).$$

This gradient has better consistency properties than the broken (element-by-element) gradient ∂_x^h, as it accounts for the jumps of its argument through the second contribution; see [16, Theorem 2.2] for further insight into this point. Taking inspiration from [30, Eq. (2.10)], we also introduce the discrete Laplace operator $\mathcal{L}_h^k : \mathbb{P}^k(\mathcal{T}_h) \to \mathbb{P}^k(\mathcal{T}_h)$ such that, for all $v_h \in \mathbb{P}^k(\mathcal{T}_h)$, $\mathcal{L}_h^k(v_h)$ solves

$$-\big(\mathcal{L}_h^k(v_h), \psi_h\big)_\Omega = a_h(1; v_h, \psi_h) \qquad \forall \psi_h \in \mathbb{P}^k(\mathcal{T}_h),$$

where the bilinear form $a_h(1; v_h, \psi_h)$ is given by (3.2) with $\kappa \equiv 1$. It can be proved that, for any $v \in H_0^1(\Omega) \cap H^{k+1}(\Omega)$, it holds

$$\inf_{v_h\in\mathbb{P}^k(\mathcal{T}_h)} \|\nabla v - \mathcal{G}_h^k(v_h)\| \lesssim h^k, \qquad \inf_{v_h\in\mathbb{P}^k(\mathcal{T}_h)} \|\triangle v - \mathcal{L}_h^k(v_h)\| \lesssim h^{k-1},$$

where $a \lesssim b$ means $a \le Cb$ with real number $C > 0$ independent of the meshsize h, and the second estimate further requires mesh quasi-uniformity.

3.4 The discrete problems

3.4.1 Model 1

The discretization of Model 1 considered here hinges on a reformulation of (7b) leading to a symmetric operator in the left-hand side. Recalling the definition (4) of the linear operator $\mathbf{T}[H, b]\cdot$, and assuming that the water depth H is bounded away from zero, it holds for any sufficiently smooth scalar-valued function v that:

$$(1+\mathbf{T}[H, b])v = (H+H\mathcal{T}[H, b])\frac{v}{H},$$

where, for any sufficiently smooth scalar-valued function w,

$$\begin{aligned}(H+H\mathcal{T}[H, b])w &= -\frac{1}{3}\partial_x(H^3\partial_x w) - \frac{H^2}{2}\partial_x w\partial_x b + \frac{1}{2}\partial_x(H^2\partial_x b\, w) + Hw(\partial_x b)^2 + Hw,\\ &= -\frac{1}{3}\partial_x(H^3\partial_x w) + \frac{1}{2}w\partial_x(H^2\partial_x b) + Hw(\partial_x b)^2 + Hw,\end{aligned}$$

since

$$-\frac{H^2}{2}\partial_x w\partial_x b = -\frac{1}{2}\partial_x(H^2\partial_x b\, w) + \frac{1}{2}\partial_x(H^2\partial_x b)w.$$

As a consequence, we can write in a more compact form

$$(H + H\mathcal{T}[H, b])w = \partial_x(-\nu[H]\partial_x w) + \beta[H, b]w, \tag{16a}$$

where

$$\nu[H] := \frac{1}{3}H^3, \qquad \beta[H, b] := H + H\partial_x H\partial_x b + \frac{1}{2}H^2\partial_x^2 b + H(\partial_x b)^2. \tag{16b}$$

Remark 2 (Sign of $\beta[H,b]$)**.** In contrast to the Modified and Optimized Green–Naghdi models detailed below, the reaction-like coefficient $\beta[H,b]$ is not necessarily positive. As a result, the discrete counterpart of the operator in the left-hand side of (16a) is not necessarily coercive (and, hence, invertible). In the numerical experiments presented below, however, no inversibility problem was encountered.

Accounting for the reformulation (16), and provided that the exact solution is sufficiently regular, Model 1 can be rewritten as

$$\partial_t \mathbf{w} + \partial_x \mathbb{f}(\mathbf{w},b) + \mathbb{d}(\mathbf{w},b) - \mathbb{b}(\mathbf{w},b) = 0, \tag{17a}$$

$$H\mathfrak{p} = \mathfrak{d} + gH\partial_x \eta, \tag{17b}$$

$$\partial_x\big(-\nu[H]\partial_x \mathfrak{p}\big) + \beta[H,b]\mathfrak{p} = gH\partial_x\eta + \mathcal{Q}_1[H,b](u), \tag{17c}$$

where (17b) has to be interpreted as the definition of the auxiliary variable $\mathfrak{p}$.

In practice, the numerical solution of (17) is sought in bounded spatial domains (which reduce to line segments since we work in 1d). To close (17), we prescribe periodic boundary conditions, obtained assuming that all the components of $\mathbf{w} = (\eta, q)$ as well as the auxiliary variable $\mathfrak{p}$ are periodic.

Let now $b_h \in \mathbb{P}^k(\mathcal{T}_h)$ denote a piecewise polynomial approximation of the topography parameterization b which can be obtained, e.g., by an L^2-orthogonal projection or by interpolation. The semi-discrete in space Discontinuous Galerkin approximation of (17) reads: Find $(\eta_h, u_h, \mathfrak{p}_h) \in (\mathbb{P}^k(\mathcal{T}_h))^3$ such that, for all $(\psi_h, \phi_h, \varphi_h) \in (\mathbb{P}^k(\mathcal{T}_h))^3$,

$$\big(\partial_t \mathbf{w}_h, \varphi_h\big)_\Omega + \big(\mathcal{A}_h(\mathbf{w}_h), \varphi_h\big)_\Omega = 0, \tag{18a}$$

$$\big(H_h\mathfrak{p}_h, \phi_h\big)_\Omega = \big(\mathfrak{d}_h, \phi_h\big)_\Omega + \big(gH_h\mathcal{G}_h^k(\eta_h), \phi_h\big)_\Omega, \tag{18b}$$

$$a_h(\nu[H_h];\mathfrak{p}_h,\psi_h) + \big(\beta_h[H_h,b_h]v_h, w_h\big)_\Omega = \big(\mathbb{Q}_h^{(1)}[H_h,b_h](\eta_h,u_h),\psi_h\big)_\Omega, \tag{18c}$$

where

(i) The discrete nonlinear operator $\mathcal{A}_h$ in (18a) is defined by

$$\big(\mathcal{A}_h(\mathbf{w}_h),\varphi_h\big)_\Omega := -\sum_{T\in\mathcal{T}_h}\big(\mathbb{f}(\mathbf{w}_h,b_h),\partial_x\varphi_h\big)_T + \sum_{T\in\mathcal{T}_h}\sum_{F\in\mathcal{F}_T}\big(\widehat{\mathbb{f}}_{TF},\varphi_h\big)_F + \big(\mathbb{d}_h,\varphi_h\big)_\Omega - \big(\mathbb{b}(\mathbf{w}_h,b_h),\varphi_h\big)_\Omega, \tag{19}$$

with discrete dispersive correction $\mathbb{d}_h := \begin{pmatrix}0 & \mathfrak{d}_h\end{pmatrix}^\intercal \in (\mathbb{P}^k(\mathcal{T}_h))^2$. Here, $\widehat{\mathbb{f}}_{TF}$ is a numerical approximation of the normal face fluxes $\mathbb{f}(\mathbf{w}_h,b_h)\cdot \mathrm{n}_{TF}$ whose precise expression will be given in Section 3.4.4 below.

(ii) The discrete linear operator $\beta_h[H_h,b_h]$ in (18c) is obtained replacing in the expression (16b) b by b_h and the gradient and Laplace operators by their discrete counterparts defined in Section 3.3:

$$\beta_h[H_h,b_h] := H_h + H_h\mathcal{G}_h^k(H_h)\mathcal{G}_h^k(b_h) + \frac{1}{2}H_h^2\mathcal{L}_h^k(b_h) + H_h\mathcal{G}_h^k(b_h)^2. \tag{20}$$

(iii) The discrete nonlinear operator $\mathbb{Q}_h^{(1)}[H_h,b_h]$ in (18c) is defined by

$$\mathbb{Q}_h^{(1)}[H_h,b_h](\eta_h,u_h) := gH_h\mathcal{G}_h^k(\eta_h) + H_h\mathcal{Q}_{1,h}[H_h,b_h](u_h).$$

where, for any $w_h \in \mathbb{P}^k(\mathcal{T}_h)$,

$$\begin{aligned}\mathcal{Q}_{1,h}[H_h,b_h](w_h) := {}& 2H_h\mathcal{G}_h^k\Big(H_h + \frac{b_h}{2}\Big)\mathcal{G}_h^k(w_h)^2 + \frac{4}{3}H_h^2\mathcal{G}_h^k(w_h)\mathcal{L}_h^k(w_h)\\ &+ H_h\mathcal{L}_h^k(b_h)w_h\mathcal{G}_h^k(w_h) + \Big(\mathcal{G}_h^k(\eta_h)\mathcal{L}_h^k(b_h) + \frac{H_h}{2}\mathcal{G}_h^k(\mathcal{L}_h^k(b_h))\Big)w_h^2.\end{aligned}$$

3.4.2 Model 2

The discretization of Model 2 hinges on a reformulation obtained in the same spirit as in the previous section. Recalling the definition (11) of $\mathbb{T}[H^b]w$, and assuming H^b bounded away from 0, for any

sufficiently smooth scalar-valued function v we note the following equivalence:

$$(1+\mathbb{T}[H^b])v = \left(H^b - \frac{1}{3}\partial_x\left((H^b)^3\partial_x\cdot\right)\right)\frac{v}{H^b} = \partial_x\left(-\nu[H^b]\partial_x\left(\frac{v}{H^b}\right)\right) + \beta[H^b,0]\frac{v}{H^b}. \tag{21}$$

Provided that the exact solution is sufficiently regular, the Modified Green–Naghdi equations (13) can be rewritten as

$$\partial_t \mathbf{w} + \partial_x \mathbb{f}(\mathbf{w},b) + \mathbb{d}(\mathbf{w},b) = \mathbb{b}(\mathbf{w},b), \tag{22a}$$
$$H^b\mathfrak{p} = \mathfrak{d} + gH\partial_x\eta, \tag{22b}$$
$$\partial_x\big(-\nu[H^b]\partial_x\mathfrak{p}\big) + \beta[H^b,0]\mathfrak{p} = H(g\partial_x\eta + \mathcal{Q}_1[H,b](u) + g\mathcal{Q}_2[H,b](\eta)) + \mathcal{Q}_3[H,H^b]H^q\mathfrak{q}), \tag{22c}$$
$$\partial_x\big(-\nu[H^b]\partial_x\mathfrak{q}\big) + \beta[H^b,0]\mathfrak{q} = gH\partial_x\eta, \tag{22d}$$

where (22b) should be intended as the definition of the auxiliary variable $\mathfrak{p}$ (the difference with respect to (17b) is that H is replaced by H^b in the left-hand side). Also in this case, we complete (22) with periodic boundary conditions, obtained assuming that all the components of $\mathbf{w} = (\eta, q)$ as well $\mathfrak{p}$ and $\mathfrak{q}$ are periodic.

Let $(b_h, H_h^b) \in (\mathbb{P}^k(\mathcal{T}_h))^2$ be broken polynomial approximations of the topography parameterization b and the water depth at rest H^b. The discrete problem reads: Find $\mathbf{w}_h = (\eta_h, q_h) \in (\mathbb{P}^k(\mathcal{T}_h))^2$ and $(\mathfrak{p}_h, \mathfrak{q}_h) \in (\mathbb{P}^k(\mathcal{T}_h))^2$ such that, for all $(\pi_h, \psi_h, \phi_h, \varphi_h) \in (\mathbb{P}^k(\mathcal{T}_h))^4$,

$$\big(\partial_t\mathbf{w}_h, \varphi_h\big)_\Omega + \big(\mathcal{A}_h(\mathbf{w}_h), \varphi_h\big)_\Omega = 0, \tag{23}$$
$$\big(\mathfrak{d}_h, \phi_h\big)_\Omega + \big(gH_h\mathcal{G}_h^k(\eta_h), \phi_h\big)_\Omega = \big(H_h^b\mathfrak{p}_h, \phi_h\big)_\Omega, \tag{24}$$
$$a_h(\nu[H_h^b];\mathfrak{q}_h,\pi_h) + \big(\beta[H_h^b,0]\mathfrak{q}_h,\pi_h\big)_\Omega = \big(gH_h\mathcal{G}_h^k(\eta_h),\pi_h\big)_\Omega, \tag{25}$$
$$a_h(\nu[H_h^b];\mathfrak{p}_h,\psi_h) + \big(\beta[H_h^b,0]\mathfrak{p}_h,\psi_h\big)_\Omega = \big(\mathbb{Q}_h^{(2)}[H_h,b_h](\eta_h,u_h),\psi_h\big)_\Omega, \tag{26}$$

where $\mathcal{A}_h$ is again defined by (29), while the discrete nonlinear operator $\mathbb{Q}_h^{(2)}[H_h,b_h]$ is such that

$$\mathbb{Q}_h^{(2)}[H_h,b_h](\eta_h,u_h) := H_h\big(g\mathcal{G}_h^k(\eta_h) + \mathcal{Q}_{1,h}[H_h,b_h](u_h) + g\mathcal{Q}_{2,h}[H_h,b_h](\eta_h)\big) + \mathcal{Q}_{3,h}[H_h,H_h^b]H_h^b\mathfrak{q}_h,$$

with, for any $w_h \in \mathbb{P}^k(\mathcal{T}_h)$,

$$\mathcal{Q}_{2,h}[H_h,b_h](w_h) := -\mathcal{G}_h^k(H_h)\mathcal{G}_h^k(w_h)\mathcal{G}_h^k(b_h) - \frac{H_h}{2}\mathcal{L}_h^k(b_h)\mathcal{G}_h^k(w_h) - \frac{H_h}{2}\mathcal{G}_h^k(b_h)^2\mathcal{G}_h^k(w_h),$$

and

$$\mathcal{Q}_{3,h}[H_h,H_h^b]w_h := \frac{1}{6}\mathcal{G}_h^k(H_h^2-(H_h^b)^2)\mathcal{G}_h^k(w_h) + \frac{1}{3}(H_h^2-(H_h^b)^2)\mathcal{L}_h^k(w_h) - \frac{1}{6}\mathcal{L}_h^k(H_h^2-(H_h^b)^2)w_h.$$

3.4.3 Model 3

The following reformulation of Model 3 is obtained using again the reformulation (21) for the operator $(1+\mathbb{T}[H^b])$ (the details are omitted for the sake of brevity):

$$\partial_t\mathbf{w}^\theta + \partial_x\mathbb{f}(\mathbf{w}^\theta,b) + \mathbb{d}^{\alpha,\gamma,\theta}(\mathbf{w}^\theta,b) = \mathbb{b}(\mathbf{w}^\theta,b), \tag{27a}$$
$$H^b\mathfrak{p} = \mathfrak{d} + \frac{1}{\alpha}gH\partial_x\eta, \tag{27b}$$
$$\begin{aligned}\partial_x\big(-\alpha(1+\theta)\nu[H^b]\partial_x\mathfrak{p}\big) + \beta[H^b,0]\mathfrak{p} &= H(\frac{1}{\alpha}g\partial_x\eta + \mathcal{Q}_1[H,b](u^\theta) + g\mathcal{Q}_2[H,b](\eta))\\ &\quad + (1+\theta)\mathcal{Q}_3[H,H^b]H^b\mathfrak{q} + \theta\mathcal{Q}_4[H]u^\theta,\end{aligned} \tag{27c}$$
$$\partial_x\big(-\alpha(1+\theta)\nu[H^b]\partial_x\mathfrak{q}\big) + \beta[H^b,0]\mathfrak{q} = gH\partial_x\eta, \tag{27d}$$
$$\partial_x\big(-\gamma\nu[H^b]\partial_x\mathfrak{m}\big) + \beta[H^b,0]\mathfrak{m} + \theta\partial_x\Big(\mathcal{D}[H]u^\theta\Big) = 0, \tag{27e}$$

where (27b) should be intended as the definition of the auxiliary variable $\mathfrak{p}$ and the dispersive correction is now defined as $\mathfrak{d}^{\alpha,\gamma,\theta}(\mathbf{w}^\theta, b) := \begin{pmatrix} H^b\mathfrak{m} \\ \mathfrak{d} \end{pmatrix}$. Periodic boundary conditions are obtained assuming that all the components of $\mathbf{w} = (\eta, q)$ as well as the auxiliary variables $\mathfrak{p}$, $\mathfrak{q}$, and $\mathfrak{m}$ are periodic.

The corresponding Discontinuous Galerkin discretization reads: Find $\mathbf{w}_h^\theta = (\eta_h, q_h^\theta) \in (\mathbb{P}^k(\mathcal{T}_h))^2$ and $(\mathfrak{p}_h, \mathfrak{q}_h, \mathfrak{m}_h) \in (\mathbb{P}^k(\mathcal{T}_h))^3$ such that, for all $(\lambda_h, \pi_h, \psi_h, \phi_h, \varphi_h) \in (\mathbb{P}^k(\mathcal{T}_h))^5$,

$$\left(\partial_t \mathbf{w}_h^\theta, \varphi_h\right)_\Omega + \left(\mathcal{A}_h^{\alpha,\theta,\gamma}(\mathbf{w}_h^\theta), \varphi_h\right)_\Omega = 0, \tag{28a}$$

$$\left(H_h^b \mathfrak{p}_h, \phi_h\right)_\Omega = \left(\mathfrak{d}_h + \frac{1}{\alpha} g H_h \mathcal{G}_h^k(\eta_h), \phi_h\right)_\Omega, \tag{28b}$$

$$a_h(\alpha(1+\theta)\nu[H_h^b]; \mathfrak{p}_h, \psi_h) + \left(\beta[H_h^b, 0]\mathfrak{p}_h, \psi_h\right)_\Omega = \left(\mathbb{Q}_h^{\alpha,\theta}, \psi_h\right)_\Omega, \tag{28c}$$

$$a_h(\alpha(1+\theta)\nu[H_h^b]; \mathfrak{q}_h, \pi_h) + \left(\beta[H_h^b, 0]\mathfrak{q}_h, \pi_h\right)_\Omega = \left(g H_h \mathcal{G}_h^k(\eta_h), \pi_h\right)_\Omega, \tag{28d}$$

$$a_h(\gamma\nu[H_h^b]; \mathfrak{m}_h, \lambda_h) + \left(\beta[H_h^b, 0] v_h, \lambda_h\right)_\Omega + \left(\theta \mathcal{G}_h\left(\mathcal{D}_h[H_h] u_h^\theta\right), \lambda_h\right)_\Omega = 0, \tag{28e}$$

where

(i) The discrete nonlinear operator $\mathcal{A}_h^{\alpha,\theta,\gamma}$ in (28a) is defined by

$$\left(\mathcal{A}_h^{\alpha,\theta,\gamma}(\mathbf{w}_h^\theta), \varphi_h\right)_\Omega := -\sum_{T\in\mathcal{T}_h} \left(\mathbb{f}(\mathbf{w}_h^\theta, b_h), \partial_x \varphi_h\right)_T + \sum_{T\in\mathcal{T}_h} \sum_{F\in\mathcal{F}_T} \left(\widehat{\mathbb{f}}_{TF}, \varphi_h\right)_F + \left(\mathfrak{d}_h^{\alpha,\theta,\gamma}, \varphi_h\right)_\Omega - \left(\mathbb{b}(\mathbf{w}_h^\theta, b_h), \varphi_h\right)_\Omega, \tag{29}$$

with discrete dispersive correction $\mathfrak{d}_h^{\alpha,\theta,\gamma} = \begin{pmatrix} H_h^b \mathfrak{m}_h \\ \mathfrak{d}_h \end{pmatrix}$. Here, $\widehat{\mathbb{f}}_{TF}$ is a numerical approximation of the normal face fluxes $\mathbb{f}(\mathbf{w}_h, b_h) \cdot \mathrm{n}_{TF}$ whose precise expression will be given in Section 3.4.4 below.

(ii) The discrete linear operator $\mathcal{D}_h[H_h]$ in (28e) is such that, for all $w_h \in \mathbb{P}^k(\mathcal{T}_h)$,

$$\mathcal{D}_h[H_h] w_h := H_h^2 \mathcal{G}_h(H_h)\mathcal{G}_h(w_h) + \frac{1}{3} H_h^3 \mathcal{L}_h(w_h).$$

(iii) The discrete quadratic operator $\mathbb{Q}_h^{\alpha,\theta}$ in (28c) is defined by

$$\begin{aligned}\mathbb{Q}_h^{\alpha,\theta} := H_h \Big(&\frac{1}{\alpha} g \mathcal{G}_h^k(\eta_h) + \mathcal{Q}_{1,h}[H_h, b_h](u_h) \\ &+ g \mathcal{Q}_{2,h}[H_h, b_h](\eta_h)\Big) + (1+\theta)\mathcal{Q}_{3,h}[H_h, H_h^b] H_h^b \mathfrak{q}_h + \theta \mathcal{Q}_{4,h}[H_h] u_h^\theta,\end{aligned}$$

where, for any $w_h \in \mathbb{P}^k(\mathcal{T}_h)$,

$$\begin{aligned}\mathcal{Q}_{4,h}[H_h] w_h := &-\mathcal{G}_h\left(\mathcal{D}_h[H_h] w_h\right) w_h + \frac{2}{3} H_h^2 \mathcal{G}_h(H_h w_h)\mathcal{L}_h(w_h) + H_h(\mathcal{G}_h(H_h)\mathcal{G}_h(H_h w_h) \\ &+ H_h \mathcal{L}_h(H_h w_h))\mathcal{G}_h(w_h) + \frac{2}{3} H_h^3 \mathcal{G}_h(w_h)\mathcal{L}_h(w_h) + H_h w_h(\mathcal{G}_h(H_h)^2 + H_h \mathcal{L}_h(H_h))\mathcal{G}_h(w_h).\end{aligned}$$

3.4.4 Interface fluxes and well-balancing

We recall here a simple choice introduced in [21] to approximate the interface fluxes $\mathbb{f}(\mathbf{w}, b) \cdot \mathrm{n}_T$, allowing to obtain a well-balanced scheme that preserves motionless steady states for Models 1, 2 and 3. Let $T \in \mathcal{T}_h$ and $F \in \mathcal{F}_T \cap \mathcal{F}_h^i$ (since we consider periodic boundary conditions, the treatment of boundary faces regarded as fictitious interfaces is essentially analogous). Denote by $\mathbf{w}^-$ and $\mathbf{w}^+$, respectively, the *interior* and *exterior* traces of $\mathbf{w}_h$ on F, with respect to the element T. Similarly, b^- and b^+ stand for the *interior* and *exterior* traces of b_h on F. We define:

$$b^* := \max(b^-, b^+), \qquad \check{b} := b^* - \max(0, b^* - \eta^-) \tag{30}$$

and

$$\check{H}^- := \max(0, \eta^- - b^*), \quad \check{H}^+ := \max(0, \eta^+ - b^*), \quad \check{\eta}^- := \check{H}^- + \check{b}, \quad \check{\eta}^+ := \check{H}^+ + \check{b},$$

leading to the new *interior* and *exterior* values:

$$\check{\mathbf{w}}^- := {}^t\left(\check{\eta}^-, \frac{\check{H}^-}{\eta^- - b^-}q^-\right), \qquad \check{\mathbf{w}}^+ := {}^t\left(\check{\eta}^+, \frac{\check{H}^+}{\eta^+ - b^+}q^+\right). \tag{31}$$

We define the numerical flux function through the interface F as follows:

$$\widehat{\mathbb{f}}_{TF} = \mathbb{f}_h(\check{\mathbf{w}}^-, \check{\mathbf{w}}^+, \check{b}, \check{b}, \mathrm{n}_{TF}) + \widetilde{\mathbb{f}}_{TF}, \tag{32}$$

where:

(i) The numerical flux function $\mathbb{f}_\mathfrak{h}$ is the global Lax–Friedrichs flux:

$$\mathbb{f}_\mathfrak{h}(\mathbf{w}^-, \mathbf{w}^+, b^-, b^+, \mathrm{n}_{TF}) := \frac{1}{2}\left(\mathbb{f}(\mathbf{w}^-, b^-)\cdot \mathrm{n}_{TF} + \mathbb{f}(\mathbf{w}^+, b^+)\cdot \mathrm{n}_{TF} - a(\mathbf{w}^+ - \mathbf{w}^-)\right),$$

with $a := \max\limits_{T\in\mathcal{T}_h}\sigma_T$ and

$$\sigma_T := \max_{\partial T}\left(\left|\frac{q_{h|T}}{\eta_{h|T} - b_{h|T}}\cdot \mathrm{n}_T\right| + \sqrt{g(\eta_{h|T} - b_{h|T})}\right).$$

(ii) $\widetilde{\mathbb{f}}_{TF}$ is a correction term defined as follows:

$$\widetilde{\mathbb{f}}_{TF} := \begin{pmatrix} 0 \\ g\check{\eta}^-(\check{b} - b^-)\end{pmatrix}. \tag{33}$$

Note that the modified interface flux (32) only induces perturbations of order $(k+1)$ when compared to the traditional interface fluxes.

3.5 Time discretization

Supplementing Models 1, 2 and 3 with an initial datum $\mathbf{w}(0,\cdot) = \mathbf{w}^0$, the time stepping is carried out using the explicit SSP-RK schemes of [26]. For $k < 3$, we consider RK-SSP schemes of order $(k+1)$. For instance, writing the semi-discrete equation (18a) in the operator form

$$\partial_t \mathbf{w}_h + \mathcal{A}_h(\mathbf{w}_h) = 0,$$

we advance from time level n to $(n+1)$ as follows with the third-order scheme as follows:

$$\begin{aligned}
\mathbf{w}_h^{n,1} &= \mathbf{w}_h^n - \Delta t^n \mathcal{A}_h(\mathbf{w}_h^n), \\
\mathbf{w}_h^{n,2} &= \frac{1}{4}(3\mathbf{w}_h^n + \mathbf{w}_h^{n,1}) - \frac{1}{4}\Delta t^n \mathcal{A}_h(\mathbf{w}_h^{n,1}), \\
\mathbf{w}_h^{n+1} &= \frac{1}{3}(\mathbf{w}_h^n + 2\mathbf{w}_h^{n,2}) - \frac{2}{3}\Delta t^n \mathcal{A}_h(\mathbf{w}_h^{n,2}),
\end{aligned}$$

where $\mathbf{w}_h^{n,i}$, $1 \le i \le 2$, are the intermediate stages, Δt^n is obtained from the CFL condition (34), and the discrete initial data $\mathbf{w}_h^0$ is defined either as the L^2-projection or interpolation on $(\mathbb{P}^k(\mathcal{T}_h))^2$ of $\mathbf{w}_0$. For $k \ge 3$, the five stages fourth order SSP-RK scheme of [49] is used (the details are omitted for the sake of simplicity) The corresponding time step Δt^n is computed adaptively using the following CFL condition (see [15]):

$$\Delta t^n = \frac{3}{4}\frac{1}{2k+1}\min_{T\in\mathcal{T}_h}\left(\frac{h_T}{\sigma_T}\right). \tag{34}$$

Remark 3. It is well known that for highly nonlinear problems, possibly with non-conservative products, and discrete formulations with very low numerical diffusion, aliasing errors may be generated, especially when high-order approximations are used and/or long time integration is considered. Numerical stability may therefore be achieved, when needed, by applying a general filtering or de-aliasing method and we use a simple (mild) exponential filter, as detailed in [28], Chapter 5.

3.6 Arbitrary order well-balancing property

We have the following result:

Proposition 4. The discrete formulation (18) together with the numerical fluxes (32) and a first order Euler time-marching algorithm preserves the motionless steady states, providing that the integrals of (18a) are exactly computed for the motionless steady states: For all $n \in \mathbb{N}$ and all $\eta^e \in \mathbb{R}$,

$$(\eta_h^n \equiv \eta^e \text{ and } q_h^n \equiv 0) \implies \left(\eta_h^{n+1} \equiv \eta^e \text{ and } q_h^{n+1} \equiv 0\right).$$

Proof. Assuming $\mathbf{w}_h \equiv \mathbf{w}_h^e := (\eta^e, 0)$, we have to show that, for all $T \in \mathcal{T}_h$ and all $\phi_h \in \mathbb{P}^k(\mathcal{T}_h)$,

$$\int_T \mathbb{f}(\mathbf{w}_h^e, b_h)\partial_x\phi_h - \sum_{F\in\mathcal{F}_T}\int_F \mathbb{f}_{TF}^e\,\phi_h - \int_T \mathbb{d}_h\phi_h + \int_T \mathbb{b}(\mathbf{w}_h^e, b_h)\phi_h = 0,$$

where $\mathbb{f}_{TF}^e$ is the interface numerical flux obtained at equilibrium. Recalling (32), and noticing that for each interface F we have $\check{\eta}^- = \check{\eta}^+ = \eta^e$ and, therefore, $\check{\mathbf{w}}^- = \check{\mathbf{w}}^+$, the consistency of the numerical flux function $\mathbb{f}_h$ implies $\mathbb{f}_{TF}^e = \mathbb{f}(\mathbf{w}^-, b^-)\cdot \mathrm{n}_{TF}$. A similar result is obtained for boundary faces considering the periodic boundary conditions. Consequently, we have

$$\int_T \mathbb{f}(\mathbf{w}_h^e, b_h)\partial_x\phi_h - \sum_{F\in\mathcal{F}_T}\int_F \mathbb{f}_{TF}^e\,\phi_h = -\int_T \partial_x\mathbb{f}(\mathbf{w}_h^e, b_h)\phi_h = -\int_T \mathbb{b}(\mathbf{w}_h^e, b_h)\phi_h,$$

assuming that the integrals are computed exactly, and observing that we locally have $\partial_x\mathbb{f}(\mathbf{w}_h^e, b_h) = \mathbb{b}(\mathbf{w}_h^e, b_h)$. For the dispersive source term, it is straightforward to check from (21) that $\mathcal{Q}_{1,h}(w_h) = 0$ whenever $w_h = 0$. Moreover, using the fact that $\mathcal{G}_h(\eta^e) = 0$ and that $[\![\mathfrak{p}_h]\!] = 0$ at boundary faces (using periodic boundary conditions), we get $\mathfrak{p}_h = 0$ as solution of (18c), and therefore $\mathfrak{d}_h = 0$ as solution of (18b). □

Following a similar reasoning, an analogous result can be obtained for Models 2 and 3. This analysis can also be extended to the high order SSP schemes of Section 3.5 exploiting the fact that the intermediate stages $\mathbf{w}_h^{n,i}$ are obtained as convex combinations of forward Euler substeps; see, e.g., [53].

4 Numerical validation and applications

In this section, we validate the discrete formulations of Section 3 through several benchmark problems. In all the test cases, the time step restriction is computed according to (34). Exploiting the symmetry of the discrete bilinear forms, the sparse linear systems are solved using a Cholesky methods. For Models 2 and 3, the matrices are built and factorized once and for all in a pre-processing step.

4.1 Accuracy validation and convergence studies

The first set of benchmark problems aim at assessing the approximation properties of the proposed discretizations, and includes comparisons among the different asymptotic models.

4.1.1 Test 1: Nonlinear shallow water equations

In this first test, we study the order of convergence for a smooth solution of the nonlinear shallow water equations (we therefore neglect the dispersive correction). We use the following bottom function and initial conditions taken from [52]:

$$h(0,x) = 5 + e^{\cos(2\pi x)},\quad q(0,x) = \sin(\cos(2\pi x)),\quad b(x) = \sin^2(\pi x),$$

defined on $\Omega = (0,1)$. Since the exact solution is not explicitly known, we use as a reference solution the one obtained for $k = 10$ on a uniform mesh containing 2048 elements. The L^2-error on the total free

surface elevation η at $t = 0.1\ s$ (when no shock wave has developed yet) is depicted in Figures 2 (for $k = 2, 3, 4, 5, 6$) and 3 (for $k = 7, 8, 9, 10$). In all the cases, the error scales as h^{k+1}.

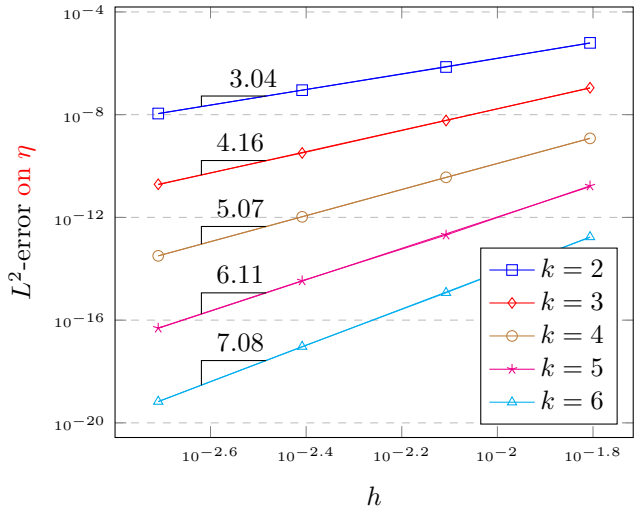

Figure 2: Test 1 - L^2-error for the total free surface elevation η at $t_{\max} = 0.1\ s$ vs. h ($k = 2, 3, 4, 5, 6$).

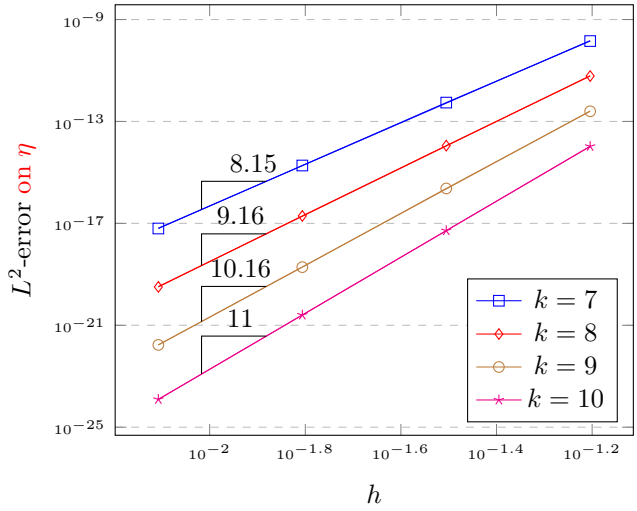

Figure 3: Test 1 - L^2-error for the total free surface elevation η at $t_{\max} = 0.1\ s$ vs. h ($k = 7, 8, 9, 10$).

4.1.2 Test 2 : Solitary waves propagation

We consider now the time evolution of the solitary wave profiles defined by (9). We recall that, while such solitary waves are exact solutions for Model 1, they only approximate solutions up to $\mathcal{O}(\mu^2)$ terms for Models 2 and 3. However, for ε and μ small enough, the profiles are expected to propagate over flat bottoms without noticeable deformations. We investigate various computational aspects: h-convergence, p-convergence, stability through long time propagation, and propagation of highly nonlinear waves. We also give an example of usage of a very high order scheme and compare the computational cost needed to achieve a required level of accuracy. We use a computational domain of $200\ m$ in length, take $h_0 = 1\ m$ as reference water depth, and $\epsilon = 0.2$ for the relative amplitude of the wave; see Figure 4 for an illustration.

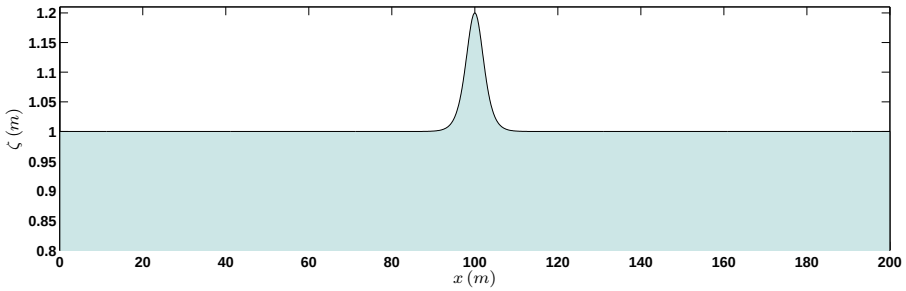

Figure 4: Test 2 - Initial free surface

h-convergence. For the discretization (18) of Model 1, we compute the L^2-error for η and q at $t = 0.1\,s$ on a sequence of refined meshes with uniform meshsize and time step refined accordingly. For $k = 2, 3, 4, 5$, we start from a uniform spatial mesh containing 2048 elements, and the computation is performed in double precision arithmetic. For $k = 6, 7, 8, 9$, we start from a uniform spatial mesh containing 512 elements, and the computations are performed in quadruple precision arithmetic, as the errors are small already on coarse meshes. The obtained results are gathered in Figures 5 ($k = 2, 3, 4, 5$) and Figure 6 ($k = 6, 7, 8, 9$). The scaling of the numerical error lies between the expected theoretical $\mathcal{O}(h^{k+\frac{1}{2}})$ estimate for a Lax–Friedrichs DG solution to a problem mainly controlled by nonlinear fluxes (see, e.g., [54]) and $\mathcal{O}(h^{k+1})$.

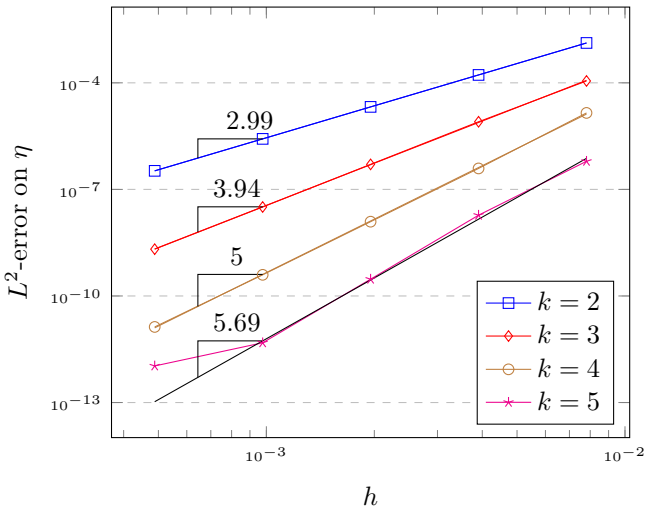

Figure 5: Test 2 - h-convergence - L^2-error for the total free surface elevation η at $t_{\max} = 0.1\,s$ vs. h ($k = 2, 3, 4, 5$).

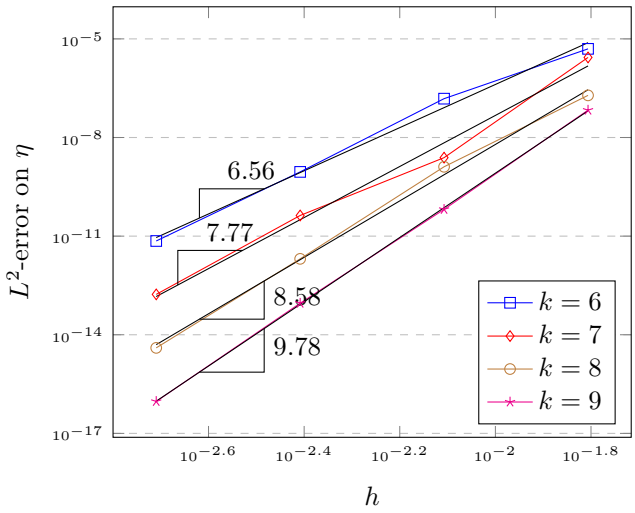

Figure 6: Test 2 - h convergence L^2-error for the total free surface elevation η at $t_{\max} = 0.1\,s$ vs. h ($k = 7, 8, 9$).

p-convergence. We next investigate the p-convergence properties of the method. In Figure 7, we display the L^2-error on the total free surface elevation η at time $t_{\max} = 0.1$ (logarithmic scale) vs. the polynomial degree (linear scale) using two uniform spatial meshes containing 512 and 1024 elements, respectively. We observe the expected exponential convergence rate with respect to k. A similar behavior is observed for the discharge, although the numerical errors are always slightly larger than those obtained for the free surface. In numerical experiments not reported here for the sake of brevity, similar convergence orders are observed for Model 2 and Model 3.

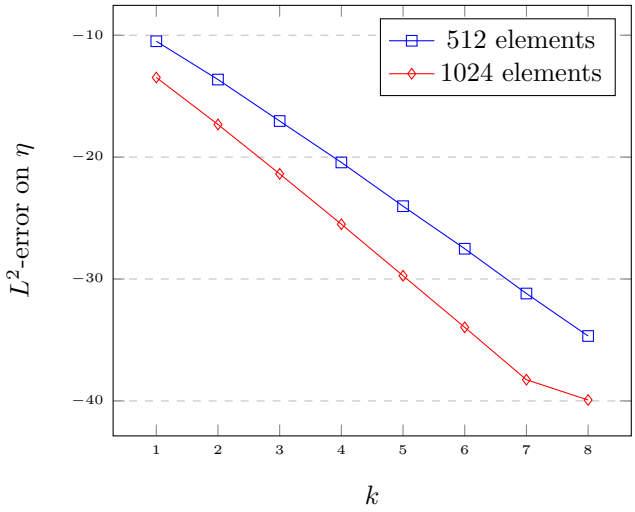

Figure 7: Test 2 - p-convergence - L^2-error for the free surface elevation at $t_{\max} = 0.1\,s$.

Energy conservation. We next study the discrete conservation of the energy invariant (10) by monitoring the following normalized error on the energy:

$$N(t) = \frac{|E(t) - E(0)|}{E(0)}. \tag{35}$$

We report in Table 1 the relative error on the computed discrete energy (35) at several times up to $t = 150\,s$ and for increasing polynomial degrees for the discretization (18) of Model 1. We observe very

good conservation properties, especially for polynomial orders greater than $k = 3$. Notice that this relative error improves by increasing the polynomial degree up to $k = 5$.

For comparison purposes, a similar study is also performed using the modified Green-Naghdi equations (Model 2). We recall that solitary waves (9) are not exact solutions of Model 2. However, for small to moderate wave amplitudes, the solitary wave profiles can be expected to propagate without too much deformation. Also, even if this modified model is not expected to exactly preserve the energy (10), we still observe good conservation of the energy in time, up to the asymptotic accuracy of the model. Note however that it does not seem possible to improve the relative error by increasing k beyond 3. To obtain a wider picture and give an assessment of the computational time savings obtained using the modified Green-Naghdi equations (Model 2), we also report in Table 1 the ratio of the CPU-time needed to compute the $150\,s$ of propagation for Model 1 ($t_{\text{cpu}\,1}$) over the CPU-time for Model 2 ($t_{\text{cpu}\,2}$), showing a dramatic improvement, especially for higher order approximations. This emphasizes here that the choice of using Model 1 or Model 2 is a matter of a trade-off, as using Model 2 allows to substantially reduce the computational time, while maintaining good conservation properties on the energy.

		k				
	t	2	3	4	5	6
Model 1	50 s	$6.04\,10^{-7}$	$2.63\,10^{-8}$	$1.83\,10^{-11}$	$3.61\,10^{-12}$	$2.58\,10^{-12}$
	100 s	$8.71\,10^{-7}$	$2.77\,10^{-8}$	$1.72\,10^{-11}$	$7.49\,10^{-12}$	$5.41\,10^{-12}$
	150 s	$1.12\,10^{-6}$	$2.90\,10^{-8}$	$2.47\,10^{-11}$	$9.75\,10^{-12}$	$8.76\,10^{-12}$
Model 2	50 s	$6.97\,10^{-7}$	$1.17\,10^{-8}$	$1.59\,10^{-8}$	$1.60\,10^{-8}$	$1.62\,10^{-8}$
	100 s	$1.07\,10^{-6}$	$1.08\,10^{-8}$	$1.78\,10^{-8}$	$1.79\,10^{-8}$	$1.83\,10^{-8}$
	150 s	$1.43\,10^{-6}$	$1.17\,10^{-8}$	$1.82\,10^{-8}$	$1.84\,10^{-8}$	$3.05\,10^{-8}$
$t_{\text{cpu}\,1}/t_{\text{cpu}\,2}$		2.6	3.1	3.5	3.9	4.4

Table 1: Test 2 - Energy conservation - Relative error on the energy for Models 1 and 2, at several times and various polynomial degrees and ratio of the corresponding CPU times.

Nonlinear waves and long time propagation. To conclude this first test case, we study the propagation of multiple nonlinear solitary waves and/or for larger time, applying a mild exponential stabilizing filter, as described in Remark 3. When carefully applied, such an anti-aliasing processes can preserve the good non-dissipating properties of the discrete formulation. As an example, we compute the propagation of a solitary wave of amplitude $\epsilon = 0.5$ up to $t = 1000\,s$, setting $k = 6$ and $h = 1\,m$. The filter parameters are set to $s = 32$, $\alpha = 16$ and $N_c = 0$. Even using such a coarse mesh, the shape of the solitary wave remains almost unchanged at $t = 1000\,s$, as shown in Figure (8) (top), corresponding to almost 20 periods around the domain. The corresponding relative error during the evolution is reported on Figure (8) (bottom), showing that the energy is conserved with at least 6 digits during the evolution.

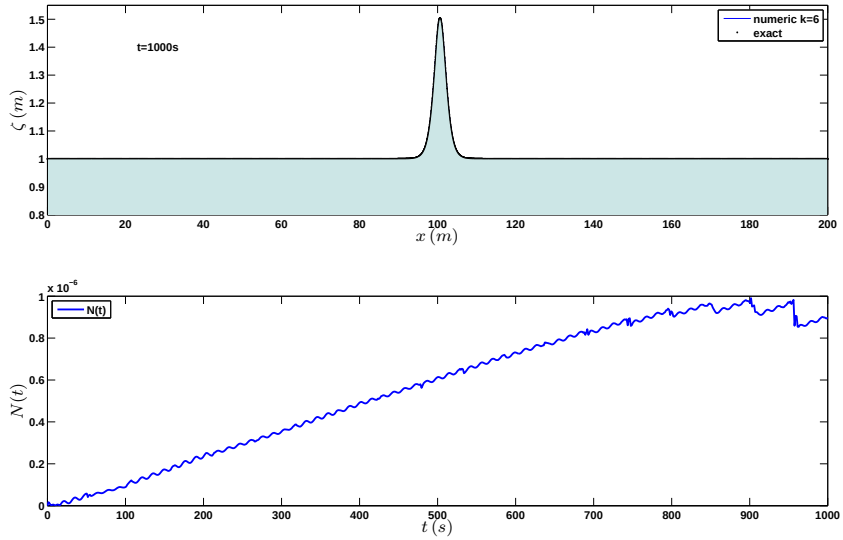

Figure 8: Test 2 - Nonlinear waves and long time propagation - Free surface at $t = 1000\,s$ (top) and time series of the energy relative error (bottom) for $\epsilon = 0.5$, $k = 6$ and $h = 1\,m$.

4.1.3 Test 3 - Cnoidal waves propagation

We recall that, whenever $b = 0$, Model 1 admits a three-parameter family of cnoidal wave solutions, see [9]. Such solutions can be formulated as follows:

$$h(x,t) = a_0 + a_1 \mathrm{dn}^2\big(\kappa(x-ct), k\big), \tag{36a}$$

$$u(x,t) = c\Big(1 - \frac{h_0}{h(x,t)}\Big), \tag{36b}$$

$$\kappa = \frac{\sqrt{3a_1}}{2\sqrt{a_0(a_0+a_1)(a_0+(1-k^2)a_1)}}, \quad c = \frac{\sqrt{ga_0(a_0+a_1)(a_0+(1-k^2)a_1)}}{h_0}, \tag{36c}$$

where $k \in [0,1]$, $a_0 > 0$, $a_1 > 0$ are real parameters, and $\mathrm{dn}(\cdot, k)$ is a Jacobi elliptic function with elliptic modulus k. The parameters of this solution can be related to physical variables in order to define (36) in terms of wave height H, wave period T, and mean water depth h_0. This can be achieved by solving the equations:

$$a_1 = \frac{H}{k^2}, \quad a_0 = h_0 - a_1\frac{E(k)}{K(k)}, \quad \hat{\omega}^2 = \frac{3\pi^2 g a_1}{4\left[a_0 K(k) + a_1 E(k)\right]^2},$$

where $\hat{\omega} = 2\pi/T$ is the angular frequency, while $K(k)$ and $E(k)$ are the complete elliptic integrals of the first and second kind respectively.

In this test case, we study the propagation of non-linear cnoidal waves defined with $H = 0.2\,m$, $h_0 = 1\,m$ and $T = 5s$. The computational domain length is set to 3 wave-lengths (which gives approximately $41.68\,m$) and we use periodic boundary conditions. In Figure 9 we show the corresponding free surface at $t = 0\,s$. A convergence study leads to sensibly similar rates as those observed for the solitary wave, although generally closer to $\mathcal{O}(h^k)$. As far as the preservation of the energy invariant is concerned, we compute the propagation up to $t = 500\,s$, using a uniform spatial mesh contanining 150 elements and for increasing polynomial orders, and report the relative error in Table 2. Again, despite the fact that (36) is not a solution for Model 2, we also compute the propagation starting from the same initial condition, and we observe very small perturbations for such moderate amplitude cnoidal waves. Again, we observe that using polynomial approximations $k \geq 3$ does not help reduce this error.

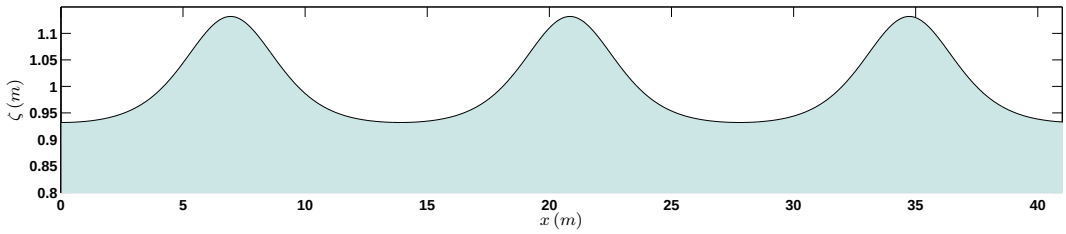

Figure 9: Test 3 - Initial free surface

		k			
	t	2	3	4	5
Model 1	100 s	$1.90\,10^{-4}$	$4.15\,10^{-6}$	$6.27\,10^{-9}$	$4.73\,10^{-9}$
	200 s	$3.31\,10^{-4}$	$5.90\,10^{-6}$	$7.57\,10^{-9}$	$5.11\,10^{-9}$
	300 s	$4.63\,10^{-4}$	$7.68\,10^{-6}$	$8.13\,10^{-9}$	$5.42\,10^{-9}$
	400 s	$5.84\,10^{-4}$	$9.46\,10^{-6}$	$8.67\,10^{-9}$	$5.69\,10^{-9}$
	500 s	$6.97\,10^{-4}$	$1.12\,10^{-5}$	$9.45\,10^{-9}$	$5.94\,10^{-9}$
Model 2	100 s	$2.70\,10^{-4}$	$1.82\,10^{-6}$	$2.66\,10^{-6}$	$2.75\,10^{-6}$
	200 s	$4.82\,10^{-4}$	$3.89\,10^{-6}$	$2.99\,10^{-6}$	$3.04\,10^{-6}$
	300 s	$6.75\,10^{-4}$	$8.51\,10^{-6}$	$2.21\,10^{-6}$	$2.26\,10^{-6}$
	400 s	$8.86\,10^{-4}$	$1.08\,10^{-5}$	$2.45\,10^{-6}$	$2.50\,10^{-6}$
	500 s	$1.01\,10^{-3}$	$1.33\,10^{-5}$	$3.01\,10^{-6}$	$3.03\,10^{-6}$
$t_{\text{cpu}\,1}/t_{\text{cpu}\,2}$		2.1	2.6	2.9	3.3

Table 2: Test 3 - Relative error on the energy for Models 1 and 2, at several times and various polynomial degrees and ratio of the corresponding CPU times.

4.1.4 Test 4 - Head-on collision of solitary waves

Another usual validation test concerns the head-on collision of two identical solitary waves propagating in opposite directions. The collision of the two waves implies a change of the nonlinear dispersion characteristics and the discrete formulation must be designed so as to ensure the equilibrium between amplitude and frequency dispersion to propagate the wave profile at constant shape and speed.

The computational domain is $\Omega = (-200\,m, 200\,m)$ and we initialize the computation with two solitary waves (9) of relative amplitude $\varepsilon = 0.2$ initially located at $x = -50\,m$ and $x = 50\,m$ and with opposite velocities, qualitatively reproducing the set up of [40]. The number of mesh elements is set to 800, corresponding to a uniform meshsize of $h = 0.5\,m$, and the polynomial order to $k = 3$. We show in Figure 10 some snapshots of the free surface at various times during the propagation with Model 1, including a zoom on the dispersive tail generated after the collision. We observe as expected that the maximum wave amplitude during the collision is slightly larger than twice the initial amplitude, in agreement with the results of [40,46]. The dispersive tail is very well reproduced, even with this relatively coarse mesh. The same computation is also performed with Model 2, and the corresponding results are shown in Figure 11. We observe very minor discrepancies on the wave profile during the propagation. The maximum amplitude during the collision is qualitatively similar to the one obtained with Model 1 and there is no phase shift. We notice, however, some variations in the oscillations of the amplitude decreasing in the dispersive tail after the collision, mainly explained by the fact that (9) is not an exact solution of Model 2.

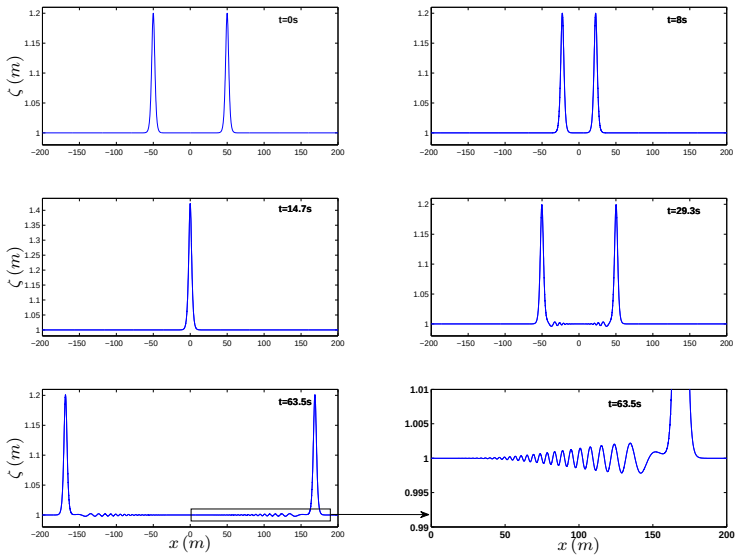

Figure 10: Test 4 - Model 1 : free surface at several time during the propagation

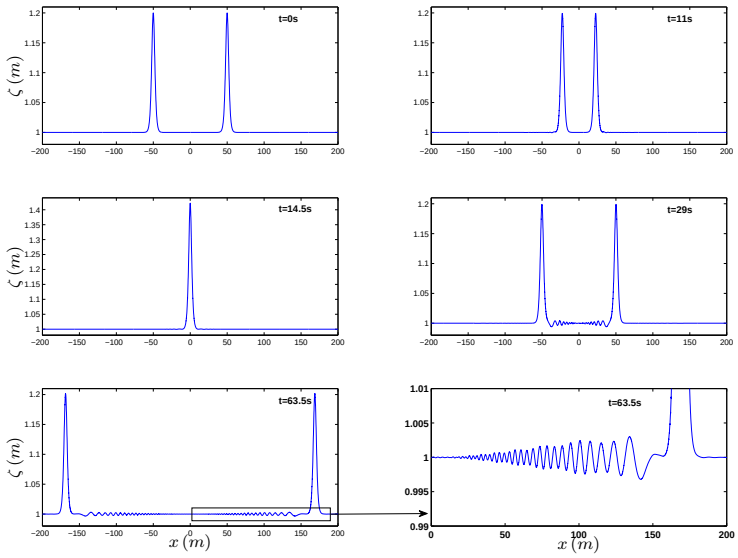

Figure 11: Test 4 - Model 2 : free surface at several time during the propagation

4.2 Applications

We consider in this section applications and comparisons with experimental data.

4.2.1 Test 5 - Reflections of solitary waves on a vertical wall

We investigate the propagation and reflection of solitary waves of various nonlinearity against a vertical wall for Model 1. In this case, periodic boundary conditions are replaced by reflective boundary condition obtained enforcing that

$$\partial_x \eta_{|\partial\Omega} = 0, \qquad q_{|\partial\Omega} = \mathfrak{p}_{|\partial\Omega} = 0.$$

Such a reflection process, which involves non-linear and dispersive interactions, has been recently used as a validation test case, e.g., in [41, 42].

We reproduce here the numerical configuration of [45], and consider a $50\,m$ long channel and a solitary wave free surface profile (9) initially located at $x_0 = 20\,m$. We use a uniform spatial mesh of 100 mesh elements, set $k = 3$, enforce reflective boundary conditions at both boundaries, and study the maximum wave amplitude at the wall located at $x = 50\,m$, for a range of wave amplitudes from $\varepsilon = 0.1$ to $\varepsilon = 0.5$. As highlighted in [10], we observe that the maximum run up of a solitary wave on a vertical wall is greater than twice the initial wave amplitude. We compare in Figure 12 our numerical results with both experimental data taken from [10, 38] and the asymptotic analytical solution for the maximum elevation proposed in [39]. We observe an excellent agreement with the asymptotic solution, and an overall good matching with the 2 sets of experimental data, very similar to the numerical results obtained in the references above.

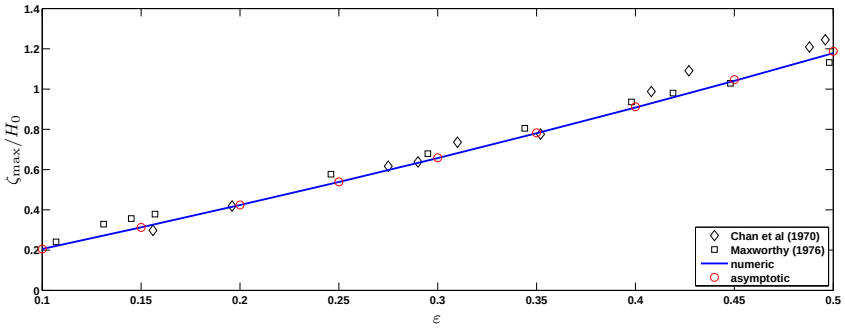

Figure 12: Test 5 - Maximum relative amplitude at the vertical wall vs. nonlinearity

Considering now a varying topography, we study the propagation and transformations of a solitary wave over a composite beach. The original experiment was performed in a tank by the U.S. Army Corps of Engineers at the Coastal Engineering Research Center in Vicksburg, Mississippi. The constructed beach consists of three piece-wise linear segments, terminated with a vertical wall on the left. The slope s of the topography is define as follows:

$$s(x) = \begin{cases} 0 \quad \text{if} \quad x \leq 15.04, \\ 1/53 \quad \text{if} \quad 15.04 \leq x \leq 19.4, \\ 1/150 \quad \text{if} \quad 19.4 \leq x \leq 22.33, \\ 1/13 \quad \text{if} \quad 22.33 \leq x \leq 23.23. \end{cases} \tag{37}$$

The schematics of the beach is shown on Figure 13.

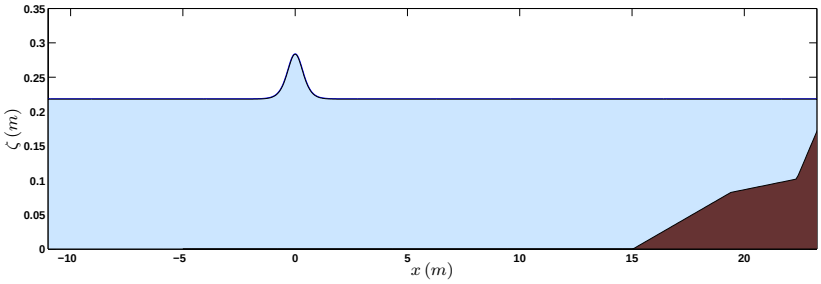

Figure 13: Shoaling and reflection of a solitary wave on a composite beach: topography and initial free surface

In the following, our numerical results are compared with experimental data measured from gages 5, 7 and 9, respectively located at $x_5 = 15.04\,m$, $x_7 = 19.4\,m$ and $x_9 = 22.33\,m$ (exactly at the locations corresponding to the slope variations). Three wave configurations were intially studied in the original experiment, with targeted solitary waves of relative amplitudes 0.05 (A), 0.3 (B) and 0.7 (C). Only (B) is computed here. Indeed, (A) involves a very small relative amplitude wave and can be quite accurately reproduced with a classical non-dispersive shallow water model, while (C) involves wave breaking during the propagation towards the wall and we choose not to include wave breaking mechanism in this work. We provide the solitary wave of targeted height, centered at $x = 0$ as the initial condition and we observe the propagation, reflection on the wall before traveling back to the inlet boundary. Experimental data are provided as time series of the wave elevation at several gages located along the wave flume. We show in Figure 14 the comparison between data and computed results for (B) at wave gages 5, 7 and 9. We obtain similar qualitative results for the remaining gages.

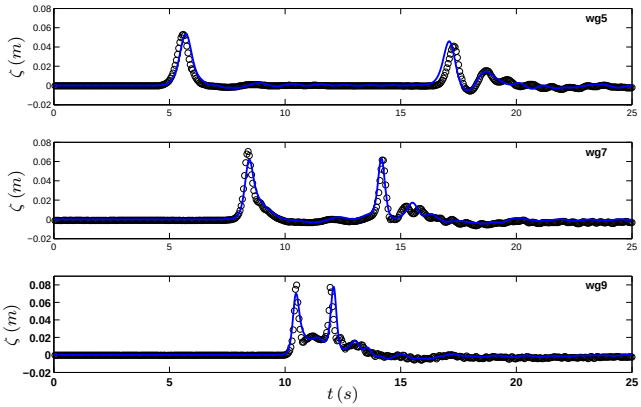

Figure 14: Shoaling and reflection of a solitary wave over a composite beach: time series of the free surface at wave gages

4.2.2 Test 6 - Propagation of periodic highly dispersive waves

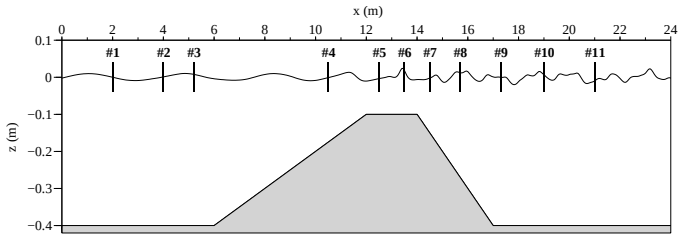

Figure 15: Test 6 - Locations of wave gages.

We focus here on the Model 3 and highlight its ability to compute the propagation and the interaction of highly dispersive waves. Using the set-up introduced in [5], and first used as a test in [19], we compute the propagation of regular periodic waves over a submerged bar, see Figure 15. For this test, we need to generate periodic waves at the left boundary, with an amplitude of $0.01\,m$, a time period of $2.02\,s$ and mean water depth $h_0 = 0.4\,m$. We therefore need to use suitable generating and absorbing boundary conditions, allowing the dissipation of the incoming waves energy together with an efficient damping of possibly non-physical reflections, and generating boundary conditions that mimic a wave generator of free surface waves. We use a relaxation method and we enforce periodic waves combined with generation/absorption by mean of a generation/relaxation zone, following the ideas of [36], using the relaxation functions described in [50], and the computational domain is locally extended to include sponge layers which may also include a generating layer.

Explicitly, the relaxed solution along the domain will take the form :

$$\mathbf{w}_{relax} = F_a \mathbf{w}_h + (1 - F_a) F_g R(t) \mathbf{w}_{imp}\,, \tag{38}$$

where F_a , F_g describe the absorption and generation profiles and R governs the time evolution of the generation process. Above, $\mathbf{w}_{imp}$ contains the enforced time series of the generated free surface. Concerning the relaxation functions, we follow [50], taking the exponential forms :

$$F_a(x) = 1 - \frac{exp\left((x_r)^n - 1)\right)}{exp(1) - 1} \quad , \quad F_g(x) = 1 - \frac{exp\left((1 - x_r)^n - 1)\right)}{exp(1) - 1}\,,$$

where $x_r = \dfrac{x - x_R}{\Delta_R}$, n is a positive parameter, and x_R, Δ_R are respectively the beginning and the width of the relaxation zone. In agreement with other works, the length of the sponge layers Δ_R is calibrated for each test case (generally 2 or 3 wavelengths); the parameter n is fixed to 3. The reader is referred to the above references for more details.

When the incident wave encounters the upward part of the bar, it shoals and steepens, which generates higher-harmonics as the nonlinearity increases. These higher-harmonics are then freely released on the downward slope, and become deep-water waves behind the bar.

Comparisons are performed between two sets of parameters ($\alpha = 1.159, \gamma = 0, \theta = 0$) and ($\alpha = 1.024, \theta = 0.188, \gamma = 0.112$) and the data taken from the experiment, for the last four wave gauges. Time series of the free surface elevation at the four last wave gauges of the experiment are plotted on Figure 16. These results are obtained using 1000 elements and $k = 2$. We observe that using the first set of parameters, the model is not able to provide an accurate free surface evolution at the wave gauge 11. This last gauge is the most discriminating one as the higher-harmonics are completely released and can be regarded as highly dispersive waves. We observe the improvements obtained using the second set of parameters at the last two wave gauges. Note that we need to introduce a substantial amount of viscosity through filtering to stabilize the computations associated with the discrete formulation for Model 3 with $\theta \neq 0$.

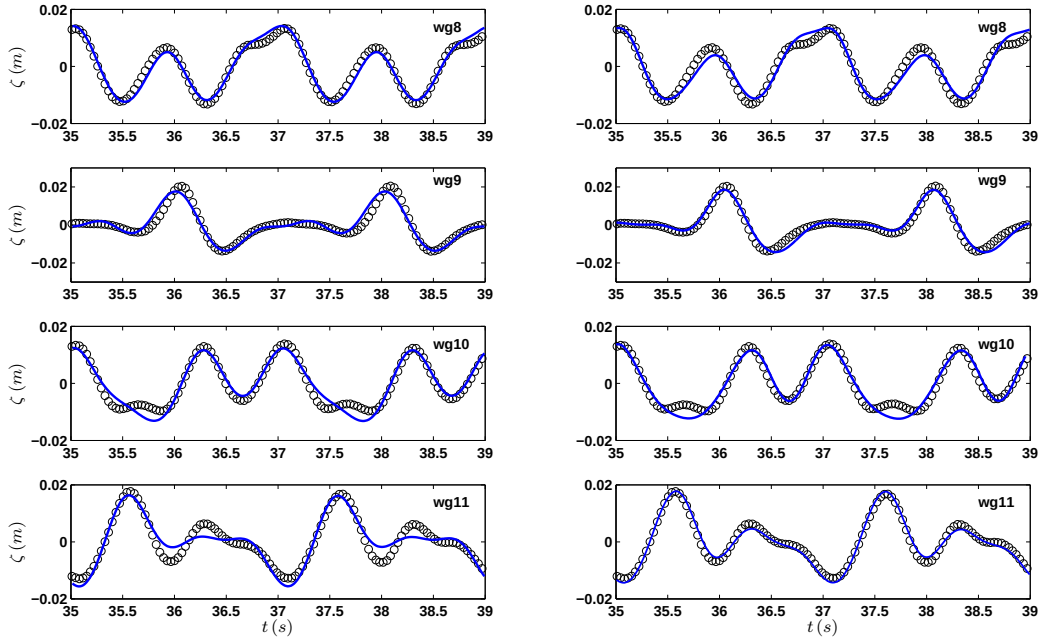

Figure 16: Test 6 - Time series of the free surface at the last 4 wage gauges. Comparison between experimental data at wave gauges (o) and numerical results (−).

Acknowledgements The authors acknowledge support from the LEFE-INSU project UHAINA and the ANR project HHOMM.

References

[1] M.B. Abbott, A.D. McGowan, and I.R. Warren. Accuracy of short wave numerical models. *J. Hydraulic Engnr.*, 110(10):1287–1301, 1984.

[2] N. Aissiouene, M.-O Bristeau, E. Godlewski, and J. and .Sainte-Marie. A combined finite volume - finite element scheme for a dispersive shallow water system. *Networks and heterogeneous media*, 11(2016):1–27, 2016.

[3] B. Alvarez-Samaniego and D. Lannes. Large time existence for 3d water-waves and asymptotics. *Invent. math.*, 171(3):485–541, 2008.

[4] J.S. Antunes do carmo, F.J. Seabra-Santos, and A.B. Almeida. Numerical solution of the generalized Serre equations with the Mac-Cormack finite-difference scheme. *Int J Numer Methods Fluids*, 16(725-738), 1993.

[5] S. Beji and J.A. Battjes. Numerical simulation of nonlinear wave propagation over a bar. *Coastal Engineering*, 23:1–16, 1994.

[6] P. Bonneton. Modelling of periodic wave transformation in the inner surf zone. *Ocean Engineering*, 34(10):1459–1471, 2007.

[7] P. Bonneton, E. Barthelemy, F. Chazel, R. Cienfuegos, D. Lannes, F. Marche, and M. Tissier. Recent advances in Serre-Green-Naghdi modelling for wave transformation, breaking and runup processes. *Eur. J. Mech. B Fluids*, 30(6):589–59, 2011.

[8] P. Bonneton, F. Chazel, D. Lannes, F. Marche, and M. Tissier. A splitting approach for the fully nonlinear and weakly dispersive Green-Naghdi model. *J. Comput. Phys.*, 230(4):1479 – 1498, 2011.

[9] J.D. Carter and R. Cienfuegos. The kinematics and stability of solitary and cnoidal wave solutions of the Serre equations. *Eur. J. Mech. B Fluids*, 30(3):259–268, 2011.

[10] R.K.C. Chan and R.L. Street. A computer study of finite-amplitude water waves. *J. Comput. Phys.*, 6:68–94, 1970.

[11] F. Chazel, D. Lannes, and F. Marche. Numerical simulation of strongly nonlinear and dispersive waves using a Green-Naghdi model. *J. Sci. Comput.*, 48:105–116, 2011.

[12] D.Y. Choi, C.H. Wu, and C.-C. Young. An efficient curvilinear non-hydrostatic model for simulating surface water waves. *Int J Numer Methods Fluids*, 66:1093–1115, 2011.

[13] R. Cienfuegos, E. Barthélemy, and P. Bonneton. A fourth-order compact finite volume scheme for fully nonlinear and weakly dispersive Boussinesq-type equations. I: Model development and analysis. *Internat. J. Numer. Methods Fluids*, 51(11):1217–1253, 2006.

[14] B. Cockburn and C.-W. Shu. The Local Discontinuous Galerkin method for time-dependent convection-diffusion systems. *SIAM J. Numer. Anal.*, 141:2440–2463, 1998.

[15] B. Cockburn and C.-W. Shu. Runge-Kutta Discontinuous Galerkin methods for convection-dominated problems. *J. Sci. Comput.*, 16(3):173–260, 2001.

[16] D. A. Di Pietro and A. Ern. Discrete functional analysis tools for discontinuous Galerkin methods with application to the incompressible Navier-Stokes equations. *Math. Comp.*, 79(271):1303–1330, 2010.

[17] D. A. Di Pietro and A. Ern. *Mathematical Aspects of Discontinuous Galerkin Methods*, volume 69 of *Mathématiques and Applications*. Springer, 2012.

[18] D. A. Di Pietro, A. Ern, and J.-L. Guermond. Discontinuous Galerkin methods for anisotropic semidefinite diffusion with advection. *SIAM J. Numer. Anal.*, 46(2):805–831, 2008.

[19] M.W. Dingemans. Comparison of computations with Boussinesq-like models and laboratory measurements. *Report H-1684, Delft Hydraulics*, 1994.

[20] M. Dryja. On discontinuous Galerkin methods for elliptic problems with discontinuous coefficients. *Comput. Methods Appl. Math.*, 3(1):76–85, 2003.

[21] A. Duran and F. Marche. Recent advances on the discontinuous Galerkin method for shallow water equations with topography source terms. *Comput. Fluids*, 101:88–104, 2014.

[22] A. Duran and F. Marche. Discontinuous-Galerkin discretization of a new class of Green-Naghdi equations. *Commun. Comput. Phys.*, 17(3):721–760, 2015.

[23] A. Duran and F. Marche. A discontinuous Galerkin method for a new class of Green-Naghdi equations on unstructured simplicial meshes. *Appl. Math. Modelling*, 45:840–864, 2017.

[24] D. Dutykh, D. Clamond, P. Milewski, and D Mitsotakis. Finite volume and pseudo-spectral schemes for fully-nonlinear 1d Serre equations. *Eur. J. Appl. Math.*, 24:761–787, 2013.

[25] A.G. Filippini, M. Kazolea, and M. Ricchiuto. A flexible genuinely nonlinear approach for wave propagation, breaking and runup. *J. Comput. Phys.*, 310:381–417, 2016.

[26] S. Gottlieb, C.-W. Shu, and Tadmor E. Strong stability preserving high order time discretization methods. *SIAM Review*, 43:89–112, 2001.

[27] A. E Green and P. M Naghdi. A derivation of equations for wave propagation in water of variable depth. *Journal of Fluid Mechanics Digital Archive*, 78(02):237–246, 1976.

[28] J. S. Hesthaven and T. Warburton. *Nodal Discontinuous Galerkin Methods. Algorithms, Analysis, and Applications*, volume 54 of *Texts in Applied Mathematics*. Springer, 2008.

[29] S. Israwi. Large time existence for 1D Green-Naghdi equations. *Nonlinear Analysis*, 74(81-93), 2011.

[30] D. Kay, V. Styles, and E. Sulli. Discontinuous Galerkin finite element approximation of the Cahn-Hilliard equation with convection. *SIAM J. Numer. Anal.*, 47(4):2660–2685, 2009.

[31] D. Lannes. *The water waves problem: mathematical analysis and asymptotics.* Number 188 in Mathematical Surveys and Monographs. American Mathematical Society, 2013.

[32] D. Lannes and P. Bonneton. Derivation of asymptotic two-dimensional time-dependent equations for surface water wave propagation. *Physics of fluids*, 21:016601, 2009.

[33] D. Lannes and F. Marche. A new class of fully nonlinear and weakly dispersive Green-Naghdi models for efficient 2d simulations. *J. Comput. Phys.*, 282:238–268, 2015.

[34] O. Le Métayer, S. Gavrilyuk, and S. Hank. A numerical scheme for the Green-Naghdi model. *J. Comput. Phys.*, 34(229):2034–2045, 2010.

[35] Q. Liang and F. Marche. Numerical resolution of well-balanced shallow water equations with complex source terms. *Advances in Water Resources*, 32(6):873 – 884, 2009.

[36] P.A. Madsen, H.B. Bingham, and H.A. Schaffer. Boussinesq-type formulations for fully nonlinear and extremely dispersive water waves: derivation and analysis. *Proc. R. Soc. A*, 459:1075–1104, 2003.

[37] L. Maojin, P. Guyenne, F. Li, and L. Xu. High order well-balanced CDG-FE methods for shallow water waves by a Green-Naghdi model. *J. Comput. Phys.*, 257, Part A(0):169 – 192, 2014.

[38] T. Maxworthy. Experiments on collisions between solitary waves. *J. Fluid Mech.*, 76:177–185, 1976.

[39] S.M. Mirie and C.H. Su. Collision between two solitary waves. Part 2. A numerical study. *J. Fluid Mech.*, 115:475–492, 1982.

[40] D. Mitsotakis, B. Ilan, and D. Dutykh. On the Galerkin/Finite-Element Method for the Serre equations. *J. Sci. Comput.*, 61(1):166–195, 2014.

[41] D. Mitsotakis, C.E. Synolakis, and M. McGuinness. A modified Galerkin/finite element method for the numerical solution of the Serre-Green-Naghdi system. *Int J Numer Methods Fluids*, 2016.

[42] N. Panda, C. Dawson, Y. Zhang, A.B. Kennedy, J.J. Westerink, and A.S. Donahue. Discontinuous Galerkin methods for solving Boussinesq-Green-Naghdi equations in resolving non-linear and dispersive surface water waves. *J. Comput. Phys.*, 273:572–588, 2014.

[43] J.D. Pearce and J.G. Esler. A pseudo-spectral algorithm and test cases for the numerical solution of the two-dimensional rotating Green-Naghdi shallow water equations. *J. Comput. Phys.*, 229:7594–7608, 2010.

[44] S. Popinet. A quadtree-adaptive multigrid solver for the Serre-Green-Naghdi equations. *J. Comput. Phys.*, 302:336–358, 2015.

[45] H. Power and T. Chwang. On reflection of a planar solitary wave at a vertical wall. *Wave Motion*, 6:183–195, 1984.

[46] M. Ricchiuto and A.G. Filippini. Upwind Residual discretization of enhanced Boussinesq equations for wave propagation over complex bathymetries. *J. Comput. Phys.*, 271:306–341, 2014.

[47] F. Serre. Contribution à l'étude des écoulements permanents et variables dans les canaux. *Houille Blanche*, 8:374–388, 1953.

[48] F. Shi, J.T. Kirby, J.C. Harris, J.D. Geiman, and S.T. Grilli. A high-order adaptive time-stepping TVD solver for Boussinesq modeling of breaking waves and coastal inundation. *Ocean Modelling*, 43-44:36–51, 2012.

[49] R.J. Spiteri and S.J. Ruuth. Non-linear evolution using optimal fourth-order strong-stability-preserving Runge-Kutta methods. *Math. Comput. Simulation*, 62(1-2):125–135, 2003.

[50] G. Wei and J. Kirby. Time-dependent numerical code for extended Boussinesq equations. *Journal of Waterway*, 121:251–261, 1995.

[51] S.B. Woo and P.L.-F. Liu. A Petrov–Galerkin finite element model for one-dimensional fully non-linear and weakly dispersive wave propagation. *Int. J. Numer. Meth. Fluids*, 37:541–575, 2001.

[52] Y. Xing and C.-W. Shu. A new approach of high orderwell-balanced finite volume weno schemes and discontinuous galerkin methods for a class of hyperbolic systems with source terms. *Commun. Comput. Phys.*, 1:100–134, 2006.

[53] Y. Xing and X. Zhang. Positivity-preserving well-balanced discontinuous Galerkin methods for the shallow water equations on unstructured triangular meshes. *J. Sci. Comput.*, 57:19–41, 2013.

[54] Q. Zhang and C.-W. Shu. Error estimates to smooth solutions of runge-kutta discontinuous galerkin methods for scalar conservation laws. *SIAM J. Numer. Anal.*, 42(2):641–666, 2004.

[55] B.B. Zhao, W.Y. Duan, and R.C. Ertekin. Application of higher-level GN theory to some wave transformation problems. *Coastal Engineering*, 83:177–189, 2014.